A Thermomechanical Framework for Analysis of Microstructural Evolution: Application to Olivine Rocks at High Temperature

Benjamin Holtzman, André Chrysochoos, Loïc Daridon

Journal of Geophysical Research: Solid Earth

RESEARCH ARTICLE
10.1029/2018JB015613

Key Points:
- Microstructural evolution in rocks at high temperature reflects strong coupling among energy storage and entropy production
- The generalized standard materials formalism for thermodynamics of irreversible processes is applied to characterize these couplings
- Energy partitioning between creep dissipation and storage in the microstructure is calculated and must be constrained by experiment

Correspondence to:
B. K. Holtzman,
benh@ldeo.columbia.edu

Citation:
Holtzman, B. K., Chrysochoos, A., & Daridon, L. (2018). A thermomechanical framework for analysis of microstructural evolution: Application to olivine rocks at high temperature. *Journal of Geophysical Research: Solid Earth*, *123*. https://doi.org/10.1029/2018JB015613

Received 8 FEB 2018
Accepted 20 AUG 2018
Accepted article online 3 SEP 2018

A Thermomechanical Framework for Analysis of Microstructural Evolution: Application to Olivine Rocks at High Temperature

B. K. Holtzman[1], **A. Chrysochoos**[2], **and L. Daridon**[2]

[1]Lamont Doherty Earth Observatory, Columbia University, New York, NY, USA, [2]Laboratoire de Mécanique et Génie Civil, Université Montpellier, CNRS, Montpellier, France

Abstract Microstructural evolution governs transient creep processes in the Earth at high temperature, on time scales from seconds to millions of years. Many experimental constraints and empirical models have been developed for discrete pieces of this problem, including flow laws and kinetic models for grain growth and dislocation recovery. We incorporate these models into a thermodynamic framework to develop a constitutive model for transient creep. The framework employed here is a branch of nonlinear thermodynamics of irreversible processes called the generalized standard materials formalism developed in solid mechanics over the last 40 years but minimally applied to geophysical problems. The generalized standard materials formalism is designed to incorporate a broad range of nonlinearity and coupling in the constitutive equations. To describe dynamic recrystallization, the model is constructed such that information propagates upward in length scale: [dislocation density → subgrain size → grain size], with each property evolving more slowly than the one below. We demonstrate that (1) the grain size-stress piezometer may contain temperature dependence below a threshold in stress, (2) the microstructural evolution is strongly temperature dependent and thus dependent on thermal boundary conditions, and (3) the fraction of mechanical work done to the system that is diverted to changing the microstructure is not a constant but is at least a function of stress, temperature, dislocation density, and grain size. This kind of thermodynamically constrained analysis can be applied to torsional deformation experiments to extract further constraints on the subprocesses of microstructural evolution and transient creep.

Plain Language Summary When rocks deform in the Earth at conditions in which they flow rather than fracture, the internal structure of the material evolves during deformation. The structure contains grains that change shape and size by a range of mechanisms, including diffusion and the motion of dislocations. How fast the structure changes determines the evolving strength of the material. This strength will control the strength of tectonic plates on a wide range of time scales, from earthquakes to the convection of the mantle. Here we develop an approach to describing this problem theoretically, using a branch of thermodynamics developed to describe the behavior of solids during deformation and the wide range of complex thermal-chemical-mechanical processes that may be occurring within the materials.

1. Introduction

The materials that constitute the Earth deform by a wide range of often-coupled processes, from fracture and granular flow to multiple diffusion and dislocation creep mechanisms. The relative rates of these processes are governed by temperature, stress, composition, and aspects of the material microstructure. Small strain transient creep occurs in response to seismic wave propagation at approximately constant microstructure and can also occur to larger strains with evolving microstructure in response to earthquakes, volcanism, ice loading, convection, and other processes. Another manifestation of microstructural change is strain localization, which may occur on length scales from millimeters to tens of kilometers and play a first-order role in controlling the strength of plate boundaries (e.g., Jin et al., 1998; Precigout et al., 2007; Rutter & Brodie, 1988; Tommasi et al., 1994; Vissers et al., 1995). Increasingly, analysis of many problems in geophysics must incorporate complex rheological behavior of the lithosphere and convecting mantle, including nonlinear flow laws, anelasticity, and microstructural evolution.

To characterize the nonlinear behavior of materials, constitutive models are composed of evolution laws and equations of state for the relevant state variables (e.g., temperature and grain size). In the geophysics literature, there has been a recent and necessary movement toward developing such constitutive models in the context of thermodynamics of irreversible processes (TIP; e.g., Bercovici et al., 2001; Cooper et al., 2016; Covey-Crump, 1994; Hackl & Renner, 2013; Herwegh et al., 2014; Karrech et al., 2011; Ricard & Bercovici, 2009; Rozel et al., 2011; Sherburn et al., 2011; Stone et al., 2004). The essential idea is to define internal state variables that regulate the storage of energy in the material structure and the dissipation of energy through various deformation mechanisms. These internal state variables generally characterize some aspect of the microstructure with varying degrees of specificity as to the physics of the structure and the mechanism (e.g., hardness, damage, dislocation structures, grain boundary structures, creep fracture, brittle fracture, and melt/fluid distributions).

Our aim here is to build a tractable TIP framework that incorporates empirical laws from laboratory studies of microstructural evolution for the analysis of experimental data and extrapolation from laboratory to Earth conditions. These TIP approaches tend to have a large number of poorly constrained parameters. To minimize this number, we incorporate as many empirical equations for subprocesses as possible. As an initial attempt, we treat a well studied but incompletely understood subset of processes, namely, the evolution of dislocation density and grain size during creep at high temperature.

1.1. Grain Size Evolution Models

Characterizing the relationship between grain size and state variables at steady state is very useful for interpreting rock structures in the field and in modeling geophysical processes that are happening much more slowly than the grain size evolution time scale. The steady state grain size reflects a complex ensemble of processes of dislocation production, organization, and recovery, interacting with grain boundary formation and migration. Steady state grain size is often believed to scale with the applied stress level (a *piezometer*; e.g., Austin & Evans, 2007; Hackl & Renner, 2013; Shimizu, 2008; Twiss, 1977) with little or no temperature dependence, which is a conundrum considering that almost all of the subprocesses have different thermally activated kinetics. In section 3.1, we discuss various models for the steady state condition. Here we briefly review the range of grain size evolution models, including ones that employ some form of TIP, and then present an overview of our approach in this paper.

Grain size evolution has been extensively studied in a wide range of rocks, beginning with crustal materials as grain size variations in ductile deformation are readily observable, in the field and laboratory. In this paper, we focus on olivine because of the enormous body of work on many aspects of its high-temperature behavior and because of its importance in controlling the dynamics of the lithosphere and convecting upper mantle. Because of the complexity of the problem and its rheological importance, a wide range of grain size evolution models has been proposed for olivine rocks (e.g., Behn et al., 2009; Braun et al., 1999; Hackl & Renner, 2013; Hall & Parmentier, 2003; Kameyama et al., 1997; Montési & Hirth, 2003; Rozel et al., 2011). Most of these models assume that grain growth and reduction are occurring simultaneously in a rock with a distribution of grain sizes, referred to as *synchronous* models by Hall and Parmentier (2003), such that the grain size (g) evolution rate $\dot{g} = \dot{g}^+ + \dot{g}^-$. Furthermore, while all use essentially the same empirical equation for thermally activated grain growth ($\dot{g}^+$), they differ widely in the form of the reduction term ($\dot{g}^-$). An important difference is whether the rate equation depends (1) solely on current values of state variables, including the current grain size (e.g., Behn et al., 2009; Hall & Parmentier, 2003; Montési & Hirth, 2003; Rozel et al., 2011) or (2) on the difference between the current and some *target* grain size (e.g., Braun et al., 1999; Kameyama et al., 1997).

All the models without a target grain size contain some ad hoc parameter that defines the partitioning of energy between storage and dissipation. The need for such a parameter was defined by Taylor and Quinney (1934), as the ratio of stored to inelastic energy, discussed in section 2.4. For example, in Hall and Parmentier (2003), the grain size reduction rate depends on the current grain size and the dislocation creep strain rate, $\dot{g}^- = -\lambda \dot{\varepsilon}_{\mathrm{dis}} g$, where λ governs how quickly the grain size reduction rate decreases with grain size and dislocation creep rate ($\dot{\varepsilon}_{\mathrm{dis}}$). An alternative model is that the grain size reduction rate (and thus the steady state grain size) scales with the total work rate (stress times strain rate, that is, power/volume, hence *wattmeter*), rather than with either stress or strain rate alone (Austin & Evans, 2007, 2009; Ricard & Bercovici, 2009; Rozel et al., 2011). In this case, λ_{AE} (our added subscript) is the fraction of energy available for deformation that is diverted into changing the grain size instead of being dissipated as dislocation creep (Austin & Evans, 2007, 2009). The value of λ is a primary unknown and is either considered to be constant (Austin & Evans, 2007, 2009) or has an assumed functional form (Herwegh et al., 2014; Ricard & Bercovici, 2009; Rozel et al., 2011). One of the

motivations for our study is to determine the partitioning of energy between storage and dissipation (i.e., the λ); the thermodynamic framework utilized here yields this partitioning as a result, not as an assumption.

1.2. Our Approach

Here we present an approach based on the continuum thermodynamics formalism (e.g., Germain et al., 1983), known as the generalized standard materials (GSM) formalism (e.g., Halphen & Nguyen, 1975) for nonlinear TIP, applied to deforming solids. This formalism has been successfully applied to detailed analysis of energy balances in localization in elastoplastic materials such as steels or pseudoelastic deformation of shape memory alloys (e.g., Chrysochoos, 1985; Chrysochoos et al., 1995, 2008). In those experiments, the primary observable is the time-varying temperature field due to heat production from irreversible processes and the distribution of rheological properties, using full-field thermal measurements. In high-temperature experiments, we cannot directly observe the temperature field (that has small perturbations at high temperature), so we focus instead on the prediction of microstructure, specifically the dislocation density and grain size.

First, we present a general overview of the GSM thermomechanical framework. In section 3, we present the experimental constraints on the physics of microstructural evolution in olivine. In section 4, we integrate these empirical constraints into the GSM, to construct a model for microstructure evolution. We limit our applications to processes at *high temperature* ($T/T_m > 0.5$, where T_m is the melting temperature for the pure phase, which for natural olivine, Fo$\sim$ 90, $T_m \approx$ 1900 °C) and *low stress* (σ/M <1E−2 where M is an elastic modulus) conditions. We incorporate two microstructural state variables (mean dislocation density and grain size). In section 6, we apply this model to existing steady state grain size data and then present the transient behavior. Torsion experiments contain much unmined information on the evolution of microstructure and rheology and have captured the onset of strain localization (e.g., Hansen et al., 2012). To extract these constraints, we develop a method for analyzing microstructural and mechanical evolution in torsion experiments.

2. TIP and the GSM

Historically, TIP was initially developed as a linear theory by Onsager, de Groot and Mazur, and Meixner (e.g., De Groot & Mazur, 1984). Linear TIP is limited to near-equilibrium open systems, in which fluxes are linear functions of thermodynamic forces (also called affinities) and can be coupled to each other via constant coefficients. State variables of number N can be treated as a set $\mathcal{S}_v$ and generally include the temperature T, the components ε_{ij} of the strain tensor, and α_k of the vector gathering any structural and compositional variables, that is, $\mathcal{S}_v = \{T, \varepsilon_{ij}, \alpha_k\}$. The fluxes or rates of change of state variables are linear functions of the thermodynamic forces vector $\boldsymbol{F}$, as constrained by the formalism. In the linear TIP, forces and fluxes of all state variables are related by a matrix $\boldsymbol{L}$ of constant coefficients associated with chemical and/or thermal diffusivities and/or viscosities, such that $\dot{\mathcal{S}}_v = \boldsymbol{LF}$. The matrix $\boldsymbol{L}$ contains the Onsager coefficients; it is constrained to be symmetric, positive and definite in order to guarantee entropy positivity. The internal entropy source is then defined as $\boldsymbol{F}.\boldsymbol{LF} \geq 0$ (where . indicates the inner product).

The linear TIP breaks down when the relationship between the forces and fluxes becomes nonlinear, requiring nonconstant coefficients, existence of thresholds, nonlinear or nonregular constitutive equations, or by other means, which are common in deforming solids. Nonlinear TIP has been developed with a range of formalisms. The branch utilized here, the GSM formalism, will be explained in detail below, following a presentation of aspects general to all branches of TIP.

2.1. Overview of Near-Equilibrium TIP

In the context of near-equilibrium TIP, the deformation process is considered to be a quasi-static, possibly dissipative process. The thermodynamic definition of a quasi-static process is one that can be approximated as a succession of equilibrium states, connected by a duration in which the state variables change and energy can be stored and dissipated, as illustrated in Figure 5a. The overall disequilibrium of the macroscopic system may contain gradients in temperature, strain, and other state properties and can be treated as a ensemble of subsystems in local equilibrium. The approximation of local equilibrium (*local state axiom*) is a statement that the subsystems are defined as each being small enough to define a single local mean temperature that is representative of the *local* thermal state, as well as for the ensemble of state variables. The absolute temperature is by construction the partial derivative of the specific internal energy with respect to the specific entropy, $T = \frac{\partial e}{\partial s} = e_{,s}$, the latter form being a shorthand we will commonly employ. The equilibrium state of each volume material element is described using a finite set of N state variables, which depict the material state and its change over time. The potential e is then a state function.

Table 1
Table of Symbols for Thermodynamic Properties

Thermodynamic quantities		
Symbol	Name	Units
e	specific internal energy	J/kg
s	specific entropy	J/K/kg
S	volumetric entropy	J/K/m^3
T	temperature	K
T_0	equilibrium temperature	K
Ψ	Helmholtz free energy potential	J/kg^3
Φ	dissipation potential	W/m^3
Φ^*	dual dissipation potential	W/m^3
$\mathcal{D}_1$	intrinsic dissipation	W/m^3
$\mathcal{D}_2$	thermal dissipation	W/m^3
A	conjugate variable ($\partial\Psi/\partial\dot{\alpha}$)	various
X	thermodynamic force ($\partial\Phi/\partial\alpha$)	various
ρ	mass density	kg/m^3
$\vec{q}$	heat flux	W/m^2
α	internal state variable	
$\mathcal{S}_v$	set of state variables	for example, $\{T, \varepsilon, \alpha_i\}$
$\dot{\mathcal{S}}_v$	set of state variable fluxes	for example, $\{\dot{T}, \dot{\varepsilon}, \dot{\alpha}_i\}$
$\mathcal{S}_X$	set of thermodynamic forces	for example, $\{X_{th}, X_v, X_{\alpha_i}\}$

2.1.1. First Law

The differential local form of the First Law of thermodynamics is written as

$$\rho\dot{e} = \boldsymbol{\sigma} : \boldsymbol{D} - div\boldsymbol{q} + r_{\text{ext}}, \tag{1}$$

where ρ is the mass density, e is the internal energy, $\boldsymbol{q}$ is the heat flux vector (inward positive), r_{ext} is any additional heat supply (e.g., external radiation energy rate or internal radioactive decay, which are not invoked in this paper), and $\boldsymbol{\sigma}$ and $\boldsymbol{D}$ are the Cauchy stress and strain rate tensors, respectively. Under the *small strain approximation* the tensor $\boldsymbol{D}$ tends toward the time derivative of the strain tensor denoted by $\dot{\varepsilon}$.

For problems of solid deformation, the Helmholtz free energy potential Ψ is more useful than e, because the directly measurable T replaces s as the state variable. The Legendre transformation from the internal to the Helmholtz free energy is defined as $\Psi = e - Ts$. This thermodynamic potential describes the same physical properties of the local equilibrium state and is now the state function, $\Psi = \Psi(\mathcal{S}_v)$, where $\mathcal{S}_v = \{T, \varepsilon_{ij}, \alpha_k\}$ is the set of state variables. Symbols are defined in Table 1.

2.1.2. Second Law

The differential, local form of the Second Law can be written as

$$\rho\dot{s} - S^{\circ}_{\text{ext}} = \rho\dot{s} - \frac{r_{\text{ext}}}{T} + div\left(\frac{\boldsymbol{q}}{T}\right) = S^{\circ}_{\text{int}} \geq 0, \tag{2}$$

where S°_{ext} is the *external entropy source*, the rate of entropy exchange with the neighboring local systems per volume, and where S°_{int} is the *internal entropy source*, the rate of internal production of entropy (e.g., Coleman & Noll, 1963; Germain et al., 1983; Tolman & Fine, 1948; Truesdell, 1969). This internal source of entropy is the difference between the overall entropy production rate per volume, $\rho\dot{s}$, and S°_{ext}, which has two contributions: (1) r_{ext} (2) a surface exchange term, the *entropy flux*, $div\left(\frac{\boldsymbol{q}}{T}\right)$, describing a conductive exchange through the surface of the system, written in a local volume form. The Second Law holds that the internal entropy source must be nonnegative for any thermodynamic process. The rate of dissipated energy, $\mathcal{D}$, is defined as $\mathcal{D} = TS^{\circ}_{\text{int}}$. (Note that the $^{\circ}$ notation indicates a path dependence to the rate quantity, such that it is not a state function, an important but subtle distinction discussed further in section 2.3.)

To define the dissipation in terms of the Helmholtz potential Ψ, the $div\left(\frac{\boldsymbol{q}}{T}\right)$ term in equation (2) is expanded and multiplied through by T, such that the Second Law becomes $\rho T\dot{s} - r_{\text{ext}} + div\,(\boldsymbol{q}) - \frac{\boldsymbol{q}}{T}\cdot\mathbf{grad}(T) \geq 0$. Then, when the First Law is substituted in, along with the time derivative of $\Psi = e - Ts$, ($\dot{\Psi} = \dot{e} - \dot{T}s - T\dot{s}$) the definition of s in terms of Ψ as $s = -\frac{\partial\Psi}{\partial T}$, and the expansion of the time derivative of $\Psi(\mathcal{S}_v)$, $\dot{\Psi} = \frac{\partial\Psi}{\partial T}\dot{T} + \frac{\partial\boldsymbol{\Psi}}{\partial\boldsymbol{\varepsilon}} : \dot{\boldsymbol{\varepsilon}} + \frac{\partial\boldsymbol{\Psi}}{\partial\boldsymbol{\alpha}}.\dot{\boldsymbol{\alpha}}$, we get

$$\mathcal{D} = \mathcal{D}_1 + \mathcal{D}_2 = \boldsymbol{\sigma} : \dot{\boldsymbol{\varepsilon}} - \rho\frac{\partial\boldsymbol{\Psi}}{\partial\boldsymbol{\varepsilon}} : \dot{\boldsymbol{\varepsilon}} - \rho\frac{\partial\boldsymbol{\Psi}}{\partial\boldsymbol{\alpha}}.\dot{\boldsymbol{\alpha}} - \frac{\boldsymbol{q}}{T}\cdot\mathbf{grad}(T) \geq 0, \tag{3}$$

Thus, the internal dissipation rate can be split into two terms, the so-called intrinsic dissipation $\mathcal{D}_1 = \boldsymbol{\sigma} : \dot{\boldsymbol{\varepsilon}} - \rho\frac{\partial\boldsymbol{\Psi}}{\partial\boldsymbol{\varepsilon}} : \dot{\boldsymbol{\varepsilon}} - \rho\frac{\partial\boldsymbol{\Psi}}{\partial\boldsymbol{\alpha}}.\dot{\boldsymbol{\alpha}}$ and the thermal dissipation, $\mathcal{D}_2 = -\frac{\boldsymbol{q}}{T}\cdot\mathbf{grad}(T)$. The intrinsic dissipation is associated with irreversible change of the microstructure (including viscous flow, plastic deformation, degradation, or damage), while the thermal dissipation is induced by heat diffusion within the system, and both are positive. The property $\mathcal{D} \equiv 0$ defines a reversible thermodynamic process. Up to this point, these discussions apply equally to linear and nonlinear TIP.

2.2. Constitutive Models in the GSM Formalism

The GSM formalism was developed to expand from the limitations of the linear TIP in applications to deforming solids. The GSM enables nonlinearity in the constitutive behavior to be incorporated by introducing the dissipation pseudopotential, Φ, which is parallel in structure to the free energy potential but describes all irreversible processes that result in entropy change (Halphen & Nguyen, 1975). In the GSM formalism, constitutive models are derived from these two thermodynamic potentials, constructed from *state laws* and *evolution laws* for the state variables that control all thermal-mechanical properties. Derived in a parallel manner, the state and evolution laws are the partial derivatives of the free energy potential and the dissipation pseudopotential, respectively. The state laws are defined as

$$\begin{cases} s = -\Psi_{,T} \\ \boldsymbol{\sigma}^r = \rho\boldsymbol{\Psi}_{,\boldsymbol{\varepsilon}} \\ \boldsymbol{A} = \rho\boldsymbol{\Psi}_{,\boldsymbol{\alpha}} \end{cases}, \tag{4}$$

where $\boldsymbol{A}$ is the vector gathering the conjugate variables associated with the internal state variables and $\boldsymbol{\sigma}^r$ is the reversible stress, whose definition is discussed below.

In the GSM formalism, the evolution equations derive from the dissipation potential $\Phi(\dot{\boldsymbol{\varepsilon}}, \dot{\boldsymbol{\alpha}}, \boldsymbol{q}; T, \boldsymbol{\varepsilon}, \boldsymbol{\alpha})$, a function of the fluxes of the state variables, with T and other state variables acting as parameters. (The semicolon indicates a distinction between the variables to the left and the parameters to the right, emphasizing that state variables can act as parameters for a given function. In this case of the dissipation potential, the variables are fluxes of state variables, and the parameters are the state variables themselves). The dissipation potential must verify some convexity properties to ensure the Clausius-Duhem inequality holds true for all thermodynamic processes:

- Convexity of $\Phi(\dot{\mathcal{S}}_v)$
- Positivity of $\Phi(\dot{\mathcal{S}}_v)$
- $\Phi(\dot{\mathcal{S}}_v = \{\mathbf{0}, \mathbf{0}, \mathbf{0}\}) = 0$

The mathematical properties (convex, positive, and minimal and zero when all fluxes are zero) of the dissipation potential ensure the positivity of $\mathcal{D}$ regardless of the thermodynamic path.

In the general case, the partial derivatives of the dissipation potential define the evolution equations:

$$\begin{cases} -\frac{\mathbf{grad}T}{T} = \boldsymbol{\Phi}_{,\boldsymbol{q}} \\ \boldsymbol{\sigma}^{ir} = \boldsymbol{\Phi}_{,\dot{\boldsymbol{\varepsilon}}} \\ \boldsymbol{X} = \boldsymbol{\Phi}_{,\dot{\boldsymbol{\alpha}}} \end{cases}, \tag{5}$$

where $\boldsymbol{X}$ is a set of *thermodynamic forces* associated with the fluxes $\dot{\boldsymbol{\alpha}}$ and $\boldsymbol{\sigma}^{\text{ir}}$ is the irreversible stress. In the GSM formalism, the stress is defined as $\boldsymbol{\sigma} = \boldsymbol{\sigma}^r + \boldsymbol{\sigma}^{\text{ir}}$ (Germain et al., 1983); the determination of which components exist depends on the choice of state variables. When the total strain rate $\dot{\boldsymbol{\varepsilon}}$ is not required to describe the irreversibility, $\boldsymbol{\sigma}^{\text{ir}} = 0$ and $\boldsymbol{\sigma} = \boldsymbol{\sigma}^r$. This stress partitioning is not common outside of the GSM formalism but

is important for establishing relations between the state and rate equations, that is, the conjugate variables and the thermodynamic forces.

To that end, from the state and evolution equations above, the intrinsic dissipation $\mathcal{D}_1$ is defined as a sum of the products of forces and fluxes of the state variables. Under the small strain hypothesis, $\mathcal{D}_1$ as derived from the Clausius-Duhem inequality reads:

$$\mathcal{D}_1 = (\boldsymbol{\sigma} - \boldsymbol{\sigma}^{\boldsymbol{r}}) : \dot{\boldsymbol{\varepsilon}} - \boldsymbol{A}\dot{\boldsymbol{\alpha}}. \tag{6}$$

It can also be derived from the dissipation potential, as

$$\mathcal{D}_1 = \boldsymbol{\sigma}^{\mathbf{ir}} : \dot{\boldsymbol{\varepsilon}} + \boldsymbol{X} \cdot \dot{\boldsymbol{\alpha}} \tag{7}$$

Inspection of the two above equations illuminates that $(\boldsymbol{\sigma} - \boldsymbol{\sigma}^{\boldsymbol{r}}) = \boldsymbol{\sigma}^{\mathbf{ir}}$, discussed above, and $-\boldsymbol{A} = \boldsymbol{X}$. The second point is essential to the energy balance and observance of the second law in the GSM: the thermodynamic force $\boldsymbol{X} = \frac{\partial \boldsymbol{\Phi}}{\partial \dot{\boldsymbol{\alpha}}}$ driving dissipation is opposite in magnitude to the conjugate variable $\boldsymbol{A} = \rho \frac{\partial \boldsymbol{\Psi}}{\partial \boldsymbol{\alpha}}$, which is the change in stored energy associated with $\boldsymbol{\alpha}$.

The GSM allows for flexibility in the form of the constitutive equations and evolution laws in that the descriptive (or *natural*) variables can be exchanged in a parallel way for the thermodynamic potentials and the dissipation pseudopotentials. Whereas the Legendre transformations allow the changing of natural state variables (i.e., T for s) for the thermodynamic potentials, the Legendre-Fenchel transformations change the descriptive variables for the dissipation potentials. For example, $\boldsymbol{X} = \frac{\partial \boldsymbol{\Phi}}{\partial \dot{\boldsymbol{\alpha}}}$, while the dual potential is such that $\dot{\boldsymbol{\alpha}} = \frac{\partial \boldsymbol{\Phi}^*}{\partial \boldsymbol{X}}$. This property is utilized in this paper.

2.3. Heat Equation and Energy Balance

The heat equation presented here is general to TIP, but in the GSM, the various components of the work rates are defined to track the removal of the energy storage rates in the microstructure from the intrinsic dissipation heat source, developed in this and the following section. To recall, the combined first and second laws (equations (1) and (3)) give, under the small strain hypothesis

$$\boldsymbol{\sigma} : \dot{\boldsymbol{\varepsilon}} - \mathcal{D}_1 = \rho \dot{e} - \rho T \dot{s} = \rho \dot{\Psi} + \rho \dot{T} s. \tag{8}$$

It is necessary to expand the entropy rate term, $\rho T \dot{s}$, in order to capture the potential couplings among the state variables, as

$$\rho T \dot{s} = -\rho T \frac{\mathrm{d}\Psi_{,T}}{\mathrm{d}t} = \underbrace{-\rho T \Psi_{,TT}}_{\rho C_{\varepsilon,\alpha}} \dot{T} - \underbrace{\left(\rho T \Psi_{,T\boldsymbol{\varepsilon}} : \dot{\boldsymbol{\varepsilon}} + \rho T \Psi_{,T\boldsymbol{\alpha}} \cdot \boldsymbol{\alpha}\right)}_{w^{\circ}_{\mathrm{the}} + w^{\circ}_{\mathrm{thc}}}, \tag{9}$$

where $C_{\varepsilon,\alpha}$ is the heat capacity at constant strain and $\boldsymbol{\alpha}$. Assuming the Fourier law, $\boldsymbol{q} = -k\mathbf{grad}(T)$, is valid, the heat equation can be written as

$$\rho C_{\varepsilon,\alpha} \dot{T} - div(\boldsymbol{k} \cdot \mathbf{grad}(T)) = \underbrace{\mathcal{D}_1 + T\boldsymbol{\sigma}^{\boldsymbol{r}}{}_{,T} : \dot{\boldsymbol{\varepsilon}} + T\boldsymbol{A}_{,T}.\dot{\boldsymbol{\alpha}}}_{w^{\circ}_h} + r_{\mathrm{ext}}, \tag{10}$$

where $\boldsymbol{k}$ is the thermal conductivity tensor and recall that $\boldsymbol{\Psi}_{,\boldsymbol{\varepsilon}} \boldsymbol{\sigma}^{\boldsymbol{r}}$ and $\boldsymbol{\Psi}_{,\boldsymbol{\alpha}} = \boldsymbol{A}$. The rate w°_h is the overall heat source induced by the deformation process. Following Chrysochoos et al. (2008), we distinguish between time derivatives and work rates, signified by $\dot{x}$ and x°, respectively, where the energy rates depend on the path; although they are rates, they are not simply the time derivatives of state functions and are not generally state functions themselves. On the left-hand side, the term $\rho C_{\varepsilon,\alpha} \dot{T}$ is the heat rate stored (or released) and $-div(\boldsymbol{k} \cdot \mathbf{grad}(T))$ represents the heat losses (or gains) by conduction. Thus, the left-hand side is a partial differential expression of the temperature.

On the right-hand side, the different heat sources are grouped: the intrinsic dissipation $\mathcal{D}_1$ with the thermomechanical coupling sources showing the temperature sensitivity of the conjugated variables $\boldsymbol{\sigma}^{\boldsymbol{r}}$ and $\boldsymbol{A}$ and the external heat supply r_{ext}. The thermomechanical coupling sources can be split into two parts: the thermoelastic source w°_{the} due to thermoelasticity and the other thermomechanical coupling sources w°_{thc} (i.e.,

Table 2
Table of Work Rate Terms in the GSM in General, and Applied to This Model

Work rate term	Symbol	GSM, general	This model
deformational	w°_{def}	$\boldsymbol{\sigma} : \dot{\boldsymbol{\varepsilon}}$	$\sigma\dot{\varepsilon}$
elastic	w°_{el}	$\boldsymbol{\sigma} : \dot{\boldsymbol{\varepsilon}}_{\text{el}}$	$\sigma(\dot{\varepsilon} - \dot{\varepsilon}_{v_i})$
viscous	w°_{vi}	$\boldsymbol{\sigma} : \dot{\boldsymbol{\varepsilon}}_{\text{vi}}$	$\sigma\dot{\varepsilon}_{v_i}$
stored	w°_{s}	$\rho\frac{\partial\Psi}{\partial\boldsymbol{\alpha}} : \dot{\boldsymbol{\alpha}} = A.\dot{\boldsymbol{\alpha}}$	$A_g\dot{g} + A_d\dot{\rho}_d$
dissipated	w°_{dis}	$w^\circ_{\text{def}} - (w^\circ_{\text{el}} + w^\circ_{\text{st}})$	$\sigma\dot{\varepsilon}_{v_i} + X_d\dot{d} + X_g\dot{g}$
inelastic	w°_{in}	$w^\circ_{\text{def}} - w^\circ_{\text{el}}$	$\sigma\dot{\varepsilon}_{v_i}$
couplings			
thermal-elastic	$w^\circ_{\text{the}} + w^\circ_{\text{thm}}$	$\rho T\frac{\partial\boldsymbol{\sigma}^r}{\partial T} : \dot{\boldsymbol{\varepsilon}} + \rho T\frac{\partial\boldsymbol{A}}{\partial T}\dot{\boldsymbol{\alpha}}$	0
elastic stored	$w^\circ_{\text{e}} + w^\circ_{\text{s}}$	$\rho\Psi_{,\boldsymbol{\varepsilon}} : \dot{\boldsymbol{\varepsilon}} + \rho\Psi_{,\boldsymbol{\alpha}}\dot{\boldsymbol{\alpha}}$	$\sigma(\dot{\varepsilon} - \dot{\varepsilon}_{v_i}) + A_d\dot{d} + A_g\dot{g}$
work rate ratios			
Taylor-Quinney	F_{w°	$\frac{w^\circ_s}{w^\circ_{in}}$	$\frac{A_d\dot{\rho}_d + A_g\dot{g}}{\sigma(\sum_i \dot{\varepsilon}_{v_i})}$
	β_{TQ}	$\frac{w^\circ_{\text{dis}}}{w^\circ_{\text{in}}} = 1 - F^\circ_w$	
	λ_{AE}	–	$\frac{A_d\dot{\rho}^+_d + A_g\dot{g}^{\text{sd}}}{\sigma(\dot{\varepsilon}_{\text{gbs}} + \dot{\varepsilon}_{\text{disl}})}$

Note. these definitions depend on the state variables and mechanical models chosen; in this model, we choose ε and ε_v, not ε_{el}. Also, we do not use w°_v in the text.

latent heat release by reaction or rate of phase change or microstructure change, the focus of this paper). It is important to point out that the two terms w°_{the} and w°_{thc} in equation (9) do not, in general, correspond directly to the coupling terms $T\boldsymbol{\sigma}^r_{,T} : \dot{\boldsymbol{\varepsilon}}$ and $T\boldsymbol{A}_{,T}.\dot{\boldsymbol{\alpha}}$; their relation depends on the chosen set of state variables and the nature of the thermomechanical coupling. The only general relation we can write relates their sums, as

$$w^\circ_{\text{the}} + w^\circ_{\text{thc}} = T\boldsymbol{\sigma}^r_{,T} : \dot{\boldsymbol{\varepsilon}} + T\boldsymbol{A}_{,T}.\dot{\boldsymbol{\alpha}}. \tag{11}$$

If we suppose that ρ and $C_{\varepsilon,\alpha}$ are material constant and if the conductivity tensor k also remains constant and isotropic, the heat equation can be simplified as

$$\rho C_{\varepsilon,\alpha}\dot{T} - k\Delta T = w^\circ_h + r_{\text{ext}}, \tag{12}$$

where ΔT is the Laplacian of T. In this paper, we solve a simplified form of this equation.

2.4. Stored Energy Ratio and Dissipation Fraction

The famous (in metallurgy) Taylor-Quinney coefficient, F_w (Taylor & Quinney, 1934), was originally defined as the ratio of stored to inelastic energy. Assuming a fixed value of this ratio has been and still is widely used for predicting mechanical behavior in engineering contexts. To reiterate, one of the aims of this paper is to assess the partitioning between stored and dissipated energy as a predictor of microstructural evolution and steady state, without assuming any ratio values a priori. Recently, Rittel and Zhang (2017) showed that this partitioning varies widely in metals and can also depend on loading geometry.

The energy partitioning is presented here starting from the rates, laid out in Table 2, followed by the corresponding path-integrated total values. In the present context, the intrinsic dissipation $\mathcal{D}_1$ is equivalent to the dissipated work rate w°_{dis}, which equals the difference between the total deformation energy rate (w°_{def}) and the sum of the elastic (w°_e) and stored (w°_s) energy rates:

$$w^\circ_{\text{def}} = \boldsymbol{\sigma} : \dot{\boldsymbol{\varepsilon}} \tag{13}$$

$$w^\circ_{\text{e}} + w^\circ_{\text{s}} = \rho\Psi_{,\boldsymbol{\varepsilon}} : \dot{\boldsymbol{\varepsilon}} + \rho\Psi_{,\boldsymbol{\alpha}} : \dot{\boldsymbol{\alpha}} \tag{14}$$

$$\mathcal{D}_1 = w^\circ_{\text{dis}} = w^\circ_{\text{def}} - (w^\circ_{\text{e}} + w^\circ_{\text{s}}). \tag{15}$$

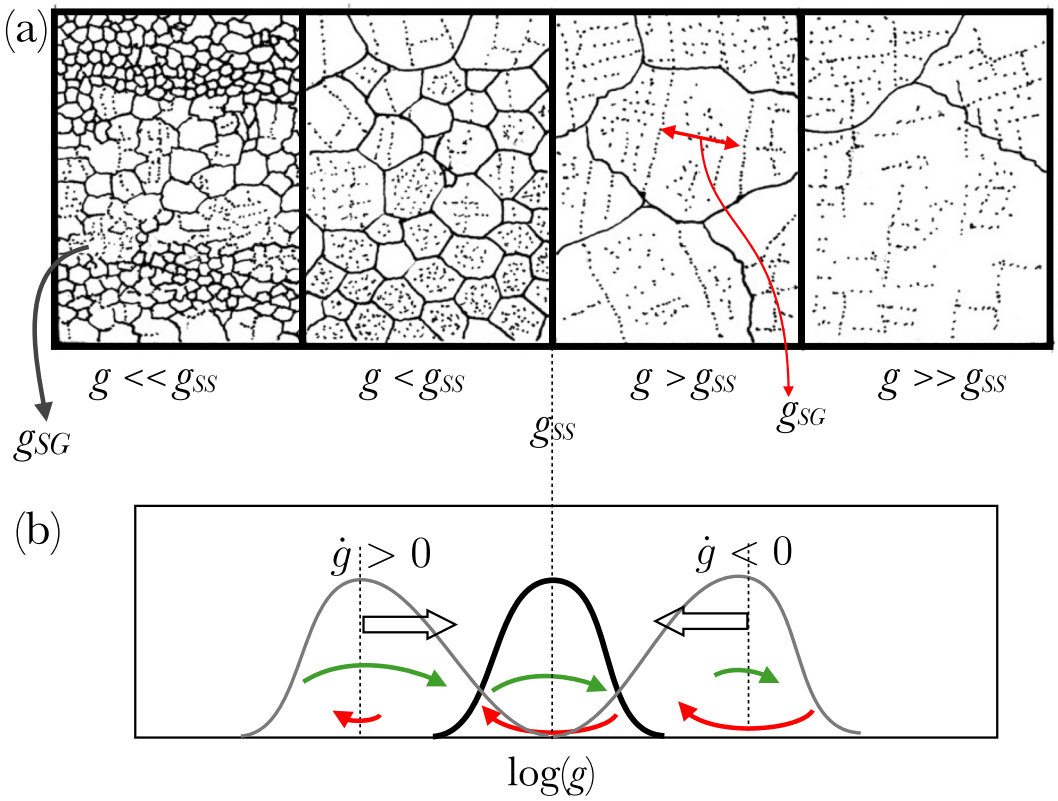

Figure 1. (a) Dots are dislocations; linear arrays of dots are subgrains; lines are grain boundaries. (b) The steady state grain size will be the mean of a distribution, in which smaller grains are growing and larger grains are being reduced during deformation. The energy dissipated when the microstructure is at steady state is accounted for by the steady state flow laws; this paper addresses the energy dissipation associated with microstructural change.

In section 4.5, it should become clear that these work rates contain a range of internal state variables that all have their own evolution equations, suggesting that the work rates are not going to be simple time derivatives of state functions. As with the heat source terms above in equation (9), it is important to point out that the two terms w_e° and w_s° in equation (13) are not necessarily equal to $\rho\Psi_{,\dot{\varepsilon}} : \dot{\varepsilon}$ and $\rho\Psi_{,\boldsymbol{\alpha}} : \dot{\boldsymbol{\alpha}}$, respectively; only the equality of the sums is true in general.

When the work rates are integrated over the path, the stored energy ratio can then be defined as

$$F_w = \frac{w_s}{w_{\text{in}}} = \frac{w_{\text{def}} - w_e - w_{\text{dis}}}{w_{\text{def}} - w_e} = \frac{w_s}{w_s + w_{\text{dis}}} \tag{16}$$

The difference, $w_{\text{def}} - w_e$, represents the inelastic work w_{in}. In the case of plastic hardening at finite strain, the elastic energy generally remains very low relative to the deformation energy, so that $F_w \approx 1 - \frac{w_{\text{dis}}}{w_{\text{def}}}$. The time derivative is

$$\dot{F}_w = \frac{\mathrm{d}}{\mathrm{d}t}\frac{w_s}{w_{\text{in}}} = \frac{w_{\text{in}} w_s^\circ - w_{\text{in}}^\circ w_s}{w_{\text{in}}^2}. \tag{17}$$

In the metallurgy literature, the stored energy ratio is often considered to be a constant ($\dot{F}_w = 0$), regardless of the initial hardening state and the loading path (typically $F_w \approx 0.1$). In this particular case, the ratio of the stored energy rate is also constant and equal to the stored energy ratio itself:

$$F_{w^\circ} = \frac{w_s^\circ}{w_{\text{in}}^\circ}. \tag{18}$$

Conversely, if the stored energy ratio changes, the integrated value is no longer equal to the stored energy rate ratio. This F_{w° is not exactly the factor λ invoked by Austin and Evans (2007, 2009) or Rozel et al. (2011) in the grain size problem, discussed below in section 4.4.3.

In many works dealing with plasticity, another Taylor-Quinney coefficient β_{TQ} is defined by Rittel (1999) as

$$\beta_{TQ} = 1 - F_{w}\circ = \frac{w^{\circ}_{dis}}{w^{\circ}_{in}} \tag{19}$$

and represents the proportion of the inelastic energy rate that is dissipated. Often supposed to be a phenomenological constant, this convenient coefficient allows estimating the dissipated work from mechanical data and the plasticity-induced self-heating, using a simple equation without a thermodynamic framework. We emphasize that within the present GSM framework, no hypotheses or assumptions on F_w and β_{TQ} are necessary; they are simply derived from the energy balance predictions since the thermodynamic and dissipation potentials are known.

3. Microstructural Evolution and Mechanical Behavior of Olivine

In this section, we lay out the experimental observations, physical models, and questions regarding microstructural evolution that motivate our approach and we seek to integrate into a thermodynamic model. During deformation at high temperature, dislocations undergo nucleation, glide, climb, annealing, and cross slip, enabling motion, strain, and organization into subgrain structures. As illustrated in Figure 1, grain growth and reduction mechanisms occur simultaneously; the evolution and emergence of a steady state mean grain size will reflect the spatiotemporal balance of a range of grain growth and reduction mechanisms. These coupled processes may be occurring simultaneously but at different rates according to an individual grain size in a heterogeneous distribution. Below, we discuss these processes in turn, building toward the question of how they interact to determine the rates of grain size evolution and a steady state grain size. We begin with a discussion of the data for steady state grain size, followed by the empirical steady state flow laws. Then we discuss dislocation-scale processes and then grain-scale processes; in each, there are processes that reduce and increase the length scale of the microstructure. Our approach is not to explicitly describe with mechanistic models all of the possible processes contributing to grain size evolution; rather, it is to provide a framework with which we can assess, primarily in experimental data, the energetic roles of the ensembles of active processes.

3.1. Steady State Grain Size

Experimental observations of recrystallized grain size or steady state grain size indicate the existence of a piezometer, a relationship between the grain size and the ambient stress level (e.g., Twiss, 1977). In Figure 2, we plot recrystallized grain size data as a function of stress, from van der Wal et al. (1993), Bystricky et al. (2000), and Karato and Toriumi (1980), which were all deformed at significantly different temperatures as indicated. These data can be fit with an empirical model of the form

$$g_{ss} = C_{pz}\sigma^{-u}, \tag{20}$$

where $C_{pz} = 0.015$ and $u = 1.33$ (van der Wal et al., 1993) or $C_{pz} = 0.02$ and $u = 1.4$ (Hirth & Kohlstedt, 2015). This piezometric relation also indicates that there is little to no temperature dependence to the olivine piezometer (Karato & Toriumi, 1980; van der Wal et al., 1993) nor for the quartz piezometer (e.g., Stipp & Tullis, 2003; Stipp et al., 2006). This observation poses a conundrum, as many of the processes involved in deformation and grain size change are known to be thermally activated, discussed below. The lack of temperature dependence of the steady state grain size could emerge if the temperature dependencies of the subprocesses are the same, while the kinetics of grain size evolution can still depend on temperature (e.g., Austin & Evans, 2007). Resolving this problem is important for understanding the extrapolation of experimental data to the Earth.

There also is ambiguity in this data set, regarding the data above about 250 MPa ($10^{2.4}$), as illustrated in Figure 2. Most of the data points are from the small grains that nucleate around the edges of coarse grains during deformation to small strains; the initial grain sizes in those experiments are far from the steady state value. In torsion experiments on olivine aggregates to very large strains, Bystricky et al. (2000) demonstrated that mean grain size continued to decrease to large strain. As illustrated in Figure 2, the final grain size (the red dot in Figure 2) was significantly smaller than the piezometer prediction. Thus, it remains ambiguous whether the reduction in grain size above about 250 MPa is due to (a) a change in mechanism of grain size reduction above some threshold in stress, similar to that observed in quartz (Kidder et al., 2016; Stipp et al., 2010), or (b)

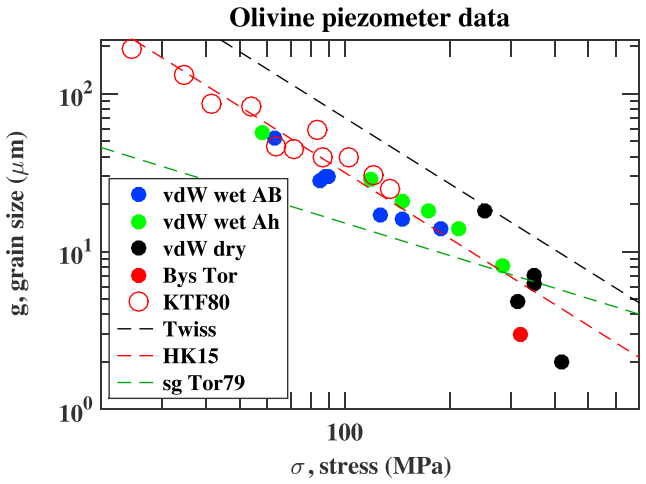

Figure 2. Recrystallized grain size data from multiple experimental laboratories. Blue dots: Anita Bay (wet) dunite; Green dots: Aheim (wet) dunite; Black dots: (dry), all from van der Wal et al. (1993); Red dot is one experiment from Bystricky et al. (2000). Hollow red circles are from Karato and Toriumi (1980). Black line is the grain size piezometer of Twiss (1977); red line is the Hirth and Kohlstedt (2015) adjustment to the Twiss piezometer; green line is the subgrain size piezometer of Toriumi (1979).

the difference between small strain recrystallized grain size and the large strain steady state grain size, with steady state grain size not yet reached for much of the data from experiments at lower stress and strain. We return to this question in section 6. As more torsion experiments are performed, we will be able to assess the kinetics of grain size evolution and characterize the steady state.

3.2. Steady State Flow Laws

At upper mantle pressures and temperatures, olivine is expected to deform under some combination of diffusion creep (through lattice and grain boundary pathways), dislocation creep, and dislocation-accommodated grain boundary sliding (GBS). The empirical flow laws for each deformation mechanism follow the same basic form (e.g., Hansen et al., 2011; Hirth & Kohlstedt, 2003), determined for steady state creep rates.

$$\dot{\varepsilon}_i(\sigma, g, T) = C^0_{v_i}|\sigma|^{n_i} g^{-m_i} \exp(-Q_i/RT)\mathrm{sgn}(\sigma) = C_{v_i}(T)|\sigma|^{n_i} g^{-m_i}\mathrm{sgn}(\sigma) \tag{21}$$

where $C_{v_i}(T) = C^0_{v_i} \exp(-Q_i/RT)$ and $i = 1$ for diffusion creep, $i = 2$ for dislocation creep and $i = 3$ for GBS creep. The g is grain size (usually d by convention, but here d is used to indicate dislocation-associated properties); Q_i is the thermal activation energy; σ is the differential stress, a scalar representative of simple stress states (tension, compression, or shear), discussed further in Appendix B. The absolute value is used, along with the sgn (sign) to ensure that the stress and strain have the same sign; for simplicity, in the rest of this paper, we simply write σ and apply only monotonous loading, though the model could be modified for cyclic or other loading paths. Effects of pressure, water fugacity, f_{H_2O} and melt fraction ϕ are well studied, but not incorporated in this paper, with parameter values are shown in Table 3. These processes are considered to act in series, as $\dot{\varepsilon} = \sum_i \dot{\varepsilon}_i$. A deformation mechanism map provides a convenient way to view the composite strain rate and the dominant deformation mechanism in each mechanism as functions of grain size and stress (Figure 3). We plot a deformation mechanism map for Hansen et al. (2011), which we will use in the calculations. Because of the grain size sensitivity of all but dislocation creep, as grain size evolves, the viscosity will change significantly. At a given temperature, the field boundary (FB) is a relationship between stress and grain size at which strain rates of two mechanisms are equal:

$$g^{\mathrm{FB}.12} = \left(\frac{C_{v_2}}{C_{v_1}}\sigma^{n-1}\right)^{1/m} = \left(\frac{C^0_{v_2}}{C^0_{v_1}}\sigma^{n-1}\exp\left(\frac{Q_2 - Q_1}{RT}\right)\right)^{1/m}, \tag{22}$$

and similarly for $g^{\mathrm{FB}.23}$ and $g^{\mathrm{FB}.13}$ (though it may be covered by $i = 2$). The role of the field boundaries will be discussed below.

3.3. Dislocations: Kinetics and Energetics

During deformation, dislocations are produced at, for example, Frank-Read sources. At high temperature in silicates, dislocation dynamics are coupled to grain size evolution. Dislocations can organize into subgrain walls by diffusive climb; when these reach a high enough misorientation angle, they become grain boundaries (i.e subgrain rotation recrystallization). Alternatively, gradients in dislocation density drive grain boundary migration to form small new grains (i.e., grain boundary migration/nucleation recrystallization). Dislocations in a crystal can be distinguished into two populations, *forest* and *mobile*, such that $\rho_d = \rho_f + \rho_m$; mobile dislocations contribute to both the stored energy and energy dissipation, while the less or immobile forest dislocations contribute to the stored energy and thus to the processes leading to grain size change. There is constant exchange between the two: dislocations nucleate, migrate, anneal away, become tangled, climb and organize into subgrain walls, and work their way free to become mobile again. Assuming an experimental sample can be perfectly quenched, the observed dislocation distribution is a snapshot; it is not always clear if this snapshot is dominated by forest or mobile dislocations. Recent models may help interpret observed structures (e.g., Boioli et al., 2015). In the formulation developed here, we do not distinguish between forest and mobile dislocations. If dislocation and GBS flow laws were expressed explicitly as a function of the mobile dislocation density, such a distinction would be useful.

Table 3
Flow Law Parameters

i, Mechanism:	$C^0_{v_i}$	n_i	m_i	Q_i
Hirth and Kohlstedt (2003)				
1: diffusion	1.5E9	1	3	375E3
2: dislocation	1.1E5	3.5	0	530E3
3: disGBS[1]	6500	3.5	2	400E3
Hansen et al. (2011)				
1: diffusion	4E7	1	3	375E3
2: dislocation	1.1E5	3.5	0	530E3
3: disGBS	6.3E4	2.9	0.73	400E3

Note. Units of A_i are ($\mu m^p/MPa^n/s$). The activation volume term is not used in this paper. Hirth and Kohlstedt values are for $T \leq 1250$ °C. disGBS = dislocation creep-accommodated grain boundary sliding.

The empirical observation that there exists a steady state dislocation density associated with a single value of stress (a piezometer) is expressed as

$$\rho_d^{ss} = \frac{\beta}{b^2}\left(\frac{\sigma}{\mu}\right)^s, \tag{23}$$

where μ is the shear modulus, b is the Burgers' vector, and the empirically determined parameters (e.g., $\beta = 1.74 \times 10^{-3}$ (m^{-2}) and $s = 1.37$; Bai & Kohlstedt, 1992). Thus, the dislocation density is apparently insensitive to temperature and chemical environment (Bai & Kohlstedt, 1992; Karato & Jung, 2003). There is also a piezometer for the subgrain size, discussed in section 3.5.4.

The internal energy per unit volume from dislocation density is modeled as

$$E_d(not\, E_\rho) = (c_1 \mu b^2)\rho_d, \tag{24}$$

where $c_1 = 1.88$, according to Hirth and Kohlstedt (2015, their α). If equation (23) is substituted in for ρ_d (not including subgrains), we obtain the energy associated with the steady state dislocation density:

$$E_d(not\, E_\rho^{ss}) = \left(\frac{c_1\beta}{\mu^{s-1}}\right)\sigma^s. \tag{25}$$

Experiments have shown that dislocation density reaches a steady state saturation in response to a stress pulse (that is then held constant) by 1–2% strain (Durham & Goetze, 1977; Durham et al., 1977). In the version of the model developed here, we calculate the evolution; we do not assume that the dislocation density is necessarily at its steady state saturation at each time step.

Similar to the grain size evolution, we use a serial or synchronous dislocation density evolution model based on the simple form discussed above, $\dot{\rho}_d = \dot{\rho}_{d^+} + \dot{\rho}_{d^-}$, where, generically, both constants can be written as $B_i = B_i^o f(T)$. The recovery term, $\dot{\rho}_{d^-} \leq 0$, has been studied in annealing experiments on olivine and an empirical form proposed (Goetze & Kohlstedt, 1973; Kohlstedt et al., 1980):

$$\dot{\rho}_{d^-} = -B^o_{d^-}\rho_d{}^q \exp\left(\frac{-(Q_{d^-} + PV^*_{d^-})}{RT}\right), \tag{26}$$

where $q = 2$, the activation energy $Q_{d^-} = 300 \pm 15$ kJ/mol, the activation volume $V^* = 11 \pm 1$ cm^3/mol (Kohlstedt et al., 1980), and P is the pressure (or mean stress, $\bar{\sigma} = (\sigma_1 + \sigma_3 + \sigma_3)/3$). $B^o_{d^-}$ is not given but is

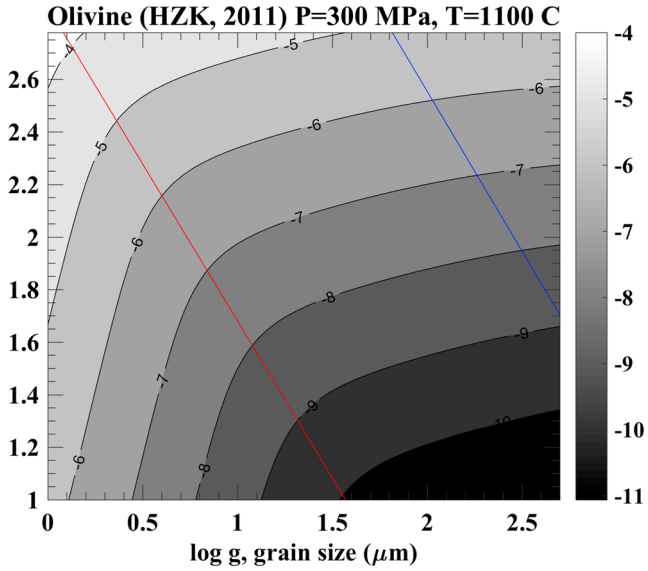

Figure 3. Deformation mechanism of flow laws from Hansen et al. (2011). Red line indicates the field boundary between diffusion and grain boundary sliding creep; blue line indicates field boundary between grain boundary sliding and dislocation creep.

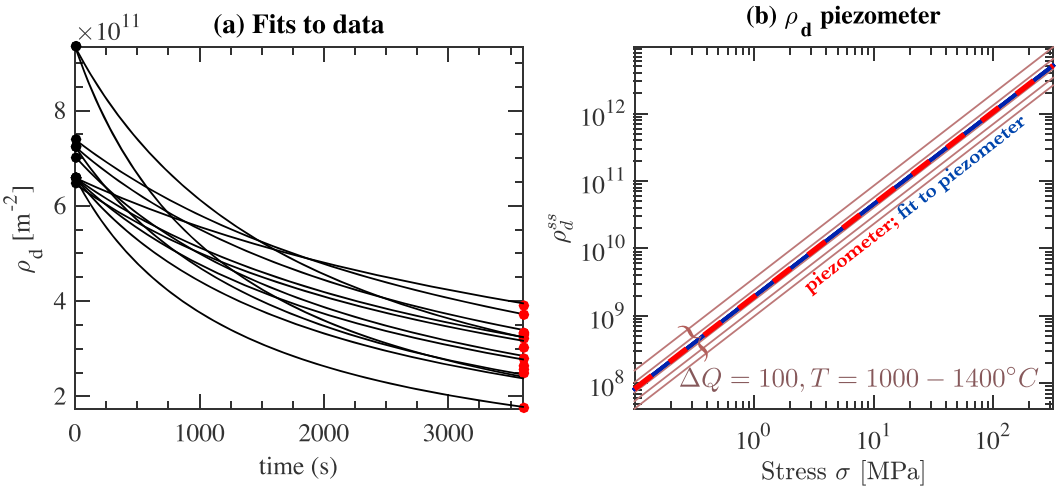

Figure 4. (a) Dislocation density annealing data and fits to the function for $\dot{\rho}^-$ (equation (26)), with $Q_{\dot{\rho}^-} = 300$ kJ/mol. (b) Reproduction of the ρ_d piezometer (thick red dashed line, equation (23), by steady state solution of two kinetic laws (equation (A1)), first assuming that their activation energies Q_d are the same (blue line) and then that the difference between the two is $\Delta Q_d = 100$ [kJ/mol]. The latter requires a value of B_{d^+} to be adjusted by a factor of 100. The lines for $\Delta Q_d = 100$ are shown over a range of 1000–1400 °C, which may fall in the range of data uncertainty and should be further explored.

determined here to be $B^o_{d^-} = 3.6\text{E}{-6}$ ($s^{-1}m^{2(q-1)}$), by fitting the data as shown in Figure 4a, neglecting the pressure dependence.

For the stress dependence of dislocation density production rate, we do not find an empirical study of the B_{d^+} term. Therefore, we propose the following form

$$\dot{\rho}_{d^+} = B^o_{d^+}\sigma^p \exp\left(\frac{-Q_{d^+}}{RT}\right) \tag{27}$$

and deduce a constraint on the magnitude of the parameters, as follows. Assuming that recovery and production are independent serial processes, we write the evolution $\dot{\rho}_d$ as

$$\dot{\rho}_d = B_{d^+}(T)\sigma^p - B_{d^-}(T)\rho_d{}^q. \tag{28}$$

In Appendix A, we derive constraints on these B_d coefficients that allow us to focus on the coefficients in the grain size evolution, but we expect that future experiments will provide much better constraints on these values.

3.4. Grain Size: Kinetics and Energetics

While the dislocation density responds relatively quickly to changes in the stress state, grain size evolves more slowly, driven by local changes in the dislocation density. Local stress may change transiently at the grain scale as the grain boundary and dislocations structures evolve. Whether local grain size is decreasing by grain boundary migration or subgrain rotation recrystallization, both mechanisms involve a local reduction of energy stored in dislocations, associated with a local increase in energy stored in grain boundaries. Similarly, grain growth over a population results in a net decrease of energy stored in grain boundaries. If net growth is occurring and grain size-sensitive creep is important, average stress may rise (if deforming under strain-controlled boundary conditions). boundary conditions), such that dislocation density will then increase. On the meaning of local in this analysis, we are assuming average values of dislocation density and grain size, where that average must be considered to be meaningful over a large enough number of grains, over a time window long enough that we can assume the average stress is constant. In this section, we discuss briefly the various processes that can be considered in the model, limiting our discussion to levels of detail appropriate to our analysis.

In the thermodynamic framework, the energy stored in the microstructure is important in the energy balance. The equation of state for the internal energy associated with grain boundaries per unit volume, E_{gb}, can be estimated as

$$E_{\text{gb}} = \frac{c_2\gamma}{g}, \tag{29}$$

where γ is the surface energy per unit area of grain boundaries (J/m^2). For spherical grains in a cubic volume and the geometric factor $c_2 = \pi$ (Austin & Evans, 2007; 2009) or $c_2 = 2$ (Hirth & Kohlstedt, 2015). It is likely that γ is a function of T (Philpot et al., 1990), but this effect is not taken into consideration as an additional nonlinearity, as it is not expected to be strong (e.g., Hirth & Kohlstedt, 2015). In the following, we discuss empirical and phenomenological models for the specific kinetic processes of grain size evolution that will eventually be coupled to changes in the stored energy.

3.4.1. Static Grain Growth

In the absence of deformation, grains will tend to grow (with smaller ones consumed) such that the mean grain size increases, driven by the reduction of surface energy of grain boundaries. The following empirical relationship is commonly used:

$$\dot{g}_{gg} = C_{gg} \exp\left(\frac{-Q_{gg}}{RT}\right) \frac{g^{1-v}}{v}, \tag{30}$$

where $v \geq 2$, depending on the mechanism of grain growth (e.g., Austin & Evans, 2009; Evans et al., 2001; Karato, 1989) and the geometry of secondary phases (e.g., Evans et al., 2001; Hiraga et al., 2010). Values for $C_{gg} = 2.0\text{E}{-2}$ (m^v/s) and $Q_{gg} = 200$ (kJ/mol) are empirically determined, with significant uncertainty (Evans et al., 2001; Karato, 1989). Note that second phases can slow this rate of growth (e.g., Tasaka & Hiraga, 2013).

3.4.2. Stress-Induced Grain Growth

Though it is infrequently considered in the grain size evolution models, deformation may enhance grain growth by at least two mechanisms. The existence of dislocations (or gradients in dislocation density) can provide a driving force for grain growth (e.g., Austin & Evans, 2009; Karato, 1989; Toriumi, 1982). If migration causes the growth of grains at the expense of smaller grains, then the mean grain size will increase. In experiments on polycrystalline aluminum, Li et al. (2016) observe much more rapid grain growth in samples with an applied stress than during static annealing. However, studies on calcite observe no obvious effect of deformation on grain growth rate (e.g., Austin & Evans, 2009). For olivine, Toriumi (1982) suggests that the effect may be very difficult to isolate. Alternatively, Kellermann Slotemaker et al. (2004), Kellermann Slotemaker and De Bresser (2006) demonstrate that grain switching during deformation can lead to enhanced grain growth. To our knowledge, no current grain size evolution models in the Earth science literature incorporate a stress-enhanced grain growth mechanism. As discussed below, we allow for the possibility but will not emphasize it until this model is used to analyze experimental data.

3.4.3. Stress-Induced Grain Size Reduction: Dynamic Recrystallization

The internal energy associated with dislocations can be transferred to the formation of increased grain boundary length, either by (1) migration of grain boundaries, rearranging and replacing regions of high dislocation density with dislocation-free regions, nucleating new grains, called nucleation recrystallization (e.g., Derby & Ashby, 1987; Guillope & Poirier, 1979; Rutter, 1995), or by (2) reorganizing dislocations into ordered subgrain walls, called subgrain rotation recrystallization (e.g., Shimizu, 1998, 2008). In both cases, while E_{gb} increases with grain size reduction, the total change depends on the subgrain and dislocation densities that can change more rapidly than grain size. In subgrain rotation recrystallization, if the thermal conditions allow sufficiently fast climb, then the tangles organize into subgrain walls. As these walls incorporate more dislocations, eventually the misorientation angle is large enough that they qualify as new recrystallized grains. The driving force for grain size reduction is the local reduction of internal energy associated with replacing dislocation tangles and subgrain walls with grain boundaries. Thus, there should be (at least) a stress dependence and a temperature dependence to the rate of grain size reduction.

We propose a stress-driven (*sd*) evolution equation for mean grain size of the following form that includes both growth and reduction:

$$\dot{g}_{sd}(T,\sigma) = C_{sd}(T)\sigma^a \left(\frac{c_g}{g^2} - \frac{c_g}{g_{att}^2}\right), \tag{31}$$

where $c_g = c_2\gamma$. The term in parentheses is the driving force calculated as the difference in thermodynamic forces between two states; these forces will be defined and derived in section 4.4.3. The g_{att} is the grain size at the attractor, determined by an equation of state, the possibilities for which are discussed below. The thermal

terms are all of the form $C(T) = C^o \exp(-Q/RT)$. We provide a stress dependence with an unknown exponent, a, to account for any stress dependence to the grain size rate that is not accounted for by the stress dependence of the dislocation density increase (also a function of stress), which might arise due to effects of stress on grain growth (section 3.4.2) or recrystallization processes; a can be determined empirically, but for now we assume $a = 1$.

The form of the driving force $\left(\frac{c_g}{g^2} - \frac{c_g}{g_{\text{att}}^2}\right)$ will be derived within the thermodynamic formalism in section 4.4.3. The use of an attractor has advantages and disadvantages: it allows the stress-driven term to change sign when grain size is above or below the attractor, as illustrated in Figure 6; however, it requires the knowledge or hypothesis of an attractor that the system somehow *knows* about. For near equilibrium, this notion is reasonable. Because this attractor and the prefactors ($C_{\text{sd}}(T)\sigma^a$) are both functions of the thermodynamic state, the direction and rate of grain size evolution can be strongly coupled and nonlinear. In our model, we allow these dependencies but do not specify a mechanism, because our aim is to constrain these rates empirically. For example, if the recrystallization mechanism changes as a function of thermodynamic state, the empirically determined parameters should change. However, the choice of g_{att} may reflect a particular mechanism; below, we describe several candidates.

3.5. Candidates for Grain Size Attractor Functions

When used as an empirical model for analysis of data, the choice of the attractor grain size g_{att} will constitute the central hypothesis of the analysis; the empirical parameters in the various aspects of the model (i.e., C_{sd}, a) will depend on the choice of g_{att}. Here we discuss four possible choices and end with the subgrain size piezometer, used in this paper.

3.5.1. Twiss Grain Size Piezometer

The model of Twiss (1977) assumes that the steady state grain size will be that at which the energy stored in the dislocation structure (presumably all dislocations, mobile and forest) is equal to that stored in the grain boundary structure. In other words, the energy stored in the microstructure seeks a state of equipartitioning between dislocations and grain boundaries, $\Delta E_{\text{disl}} = \Delta E_{\text{gb}}$, where the Δ indicates the change in internal energy due to the presence of the structures. Equating equations (25) and (29) and rearranging as a function of stress,

$$g_{\text{ss}}^{\text{Tw}} = \left(\frac{c_2}{c_1}\frac{\gamma \mu^{s-1}}{\beta}\right)\sigma^{-s}. \tag{32}$$

This equation implies that the exponents $s = u$ (and indeed $1.37 \approx 1.4$). Using the Twiss model as the attractor implies that the system will organize toward a state of equipartitioning of stored energy among the two dominant aspects of the microstructure, dislocations, and grain size. One compelling feature of this model is that it explains the temperature independence of the piezometer in that the relative energies only depend on stress; for olivine, neither energies have significant temperature dependence (Hirth & Kohlstedt, 2015). A recent analysis of creep and grain size data for olivine (Hirth & Kohlstedt, 2015) reduces the grain size predictions of the Twiss model by a factor of 0.45, as illustrated in Figure 2. Shimizu (2008) argues that the Twiss model works better for subgrain size than grain size.

3.5.2. FB Hypothesis

In the FB hypothesis (de Bresser et al., 1998, 2001), the steady state grain size will tend to fall near the boundary between diffusion and dislocation creep fields. In this hypothesis, the FB acts as an attractor because the grain size will continue to reduce in the dislocation creep regime, but once in the diffusion creep regime, the production of dislocations will diminish and thus the grain size reduction rate; surface energy-driven grain growth will then cause grains to grow back up toward the dislocation creep field, as implied in Figure 1. Precigout et al. (2007) proposed that the FB hypothesis is consistent with the location of the empirical piezometer if the FB is that between diffusion creep and dislocation-accommodated GBS creep, using the Hirth and Kohlstedt (2003) flow laws. Subsequently, the Hansen et al. (2011) flow laws provide a significantly different location for the diffusion-GBS FB.

As an attractor, the FB hypothesis implies that the system will organize toward a state of equipartitioning between two dominant dissipative creep mechanisms. Because the position of the FB is temperature dependent, the FB hypothesis suggests a moderate temperature dependence of the steady state grain size or requires another explanation for a lack of temperature sensitivity. Using the FB hypothesis as an attractor would introduce another degree of thermomechanical coupling.

The wattmeter model of Austin and Evans (2007, 2009) is something of a hybrid model; because the grain size reduction rate depends on the dislocation creep rate, the reduction decreases as the grain size enters the diffusion creep field, and the static grain growth can take over.

3.5.3. Kinetic Models

Another class of models for steady state grain size pose that it occurs when the rate of grain growth is balanced by the rate of nucleation of new small grains (e.g., Derby, 1991; Derby & Ashby, 1987; Shimizu, 1998, 2008). Because these kinetic processes are temperature dependent, weak to moderate temperature dependence of the steady state grain size is expected. These models are focused more on nucleation recrystallization. Since the driving force for these kinetic processes is the reduction of some spatial and/or temporal difference in internal energy (elastic energies around dislocations or surface energy of grain boundaries), the energetic and kinetic approaches should eventually converge. Here we focus on subgrain rotation recrystallization.

3.5.4. Subgrain Size Piezometer

The subgrain size is a natural attractor when the recrystallization mechanism is subgrain rotation; by definition, new grains nucleate at this grain size. Conceptually, the justification is the same as for the Twiss grain size piezometer, which the steady state relationship occurs when energy stored in the subgrain structure equals that in the mobile dislocations within subgrain interiors. In line with Twiss's (1977) argument, the steady state mean grain size will not likely be exactly the grain size of the attractor, because of grain growth during deformation, as illustrated in Figure 2. Several subgrain piezometers, $g_{sg}(\sigma)$, exist for olivine (e.g., Karato & Toriumi, 1980; Toriumi, 1979; Twiss, 1977). We use the empirical Toriumi (1979) subgrain piezometer (plotted in Figure 2) because it is provided in the form $g_{sg}(\rho_d)$:

$$g_{sg}(\rho_d) = \frac{c_{sg}}{\sqrt{\rho_d}}, \tag{33}$$

where $c_{sg} = 15$ is a phenomenological constant considered to be independent of the temperature, recently demonstrated to agree well with both experimental and natural samples (Hansen & Warren, 2015). *In this paper, we use this subgrain size piezometer as the attractor, such that* $g_{att} = g_{sg}(\rho_d)$. There is a strong physical justification for this choice: The attractor depends on the dislocation density (which is a function of stress and temperature) and thus induces a strong coupling between the evolution of the two microstructural state variables. However, this choice is specific to this mechanism; if a system enters a grain nucleation recrystallization regime, this choice of g_{att} could be misleading. We also note that we are implicitly assuming that the distribution of g_{sg} can be defined by a mean value, as we do with the grain size, reflecting the idea that the distribution evolves in a self-similar way with changing stress state (Cooper et al., 2016; Stone et al., 2004).

3.6. Synthesis

Here we bring together these various empirical constraints and models and present the design of the study. The model developed below uses two microstructural state variables, mean grain size, and mean dislocation density. The motivation of the subsequent thermodynamic framework is to track energy partitioning among that dissipated in purely irreversible creep and that which goes into changing the microstructure. Because the processes involved are nonuniformly temperature sensitive, the temperature evolution must be tracked and the sensitivity to the thermal conditions explored. Consistent with our physical view, the evolution of the dislocation density is the driver for grain size evolution; ρ_d evolves relatively quickly and the grain size lags behind: $[\rho_d \rightarrow g_{sg} \rightarrow g]$, in sequence of decreasing rates of kinetic response to changing stress. The time scale of that lag is governed by temperature and stress; we consider these to be the least well constrained parameters in this model. The grain size is responding to the attractor defined by the subgrain size ($g_{att} = g_{sg}$), which is a function of the current dislocation density. In the next section, we incorporate these empirical pieces into the GSM framework.

4. GSM Formalism Applied to Microstructural Evolution in Olivine

Here we apply the GSM formalism to the problem of microstructural evolution during creep, as illustrated conceptually in Figure 5. The state variables for this system are incorporated into the set $\mathcal{S}_v = \{T, \varepsilon, \varepsilon_{v_i}, \rho_d, g\}$. The system is open to mechanical work and heat flux but closed to mass flux (Figure 5b), and internally, energy is partitioned into a portion stored in the elasticity and the microstructure and a portion dissipated by creep (Figure 5c). The basic mechanical behavior is a Maxwell viscoelastic model of a spring and nonlinear dashpots in series, such that the strain is decomposed into a contribution from the spring and the dashpots ($\varepsilon = \varepsilon_e + \varepsilon_{v_i}$),

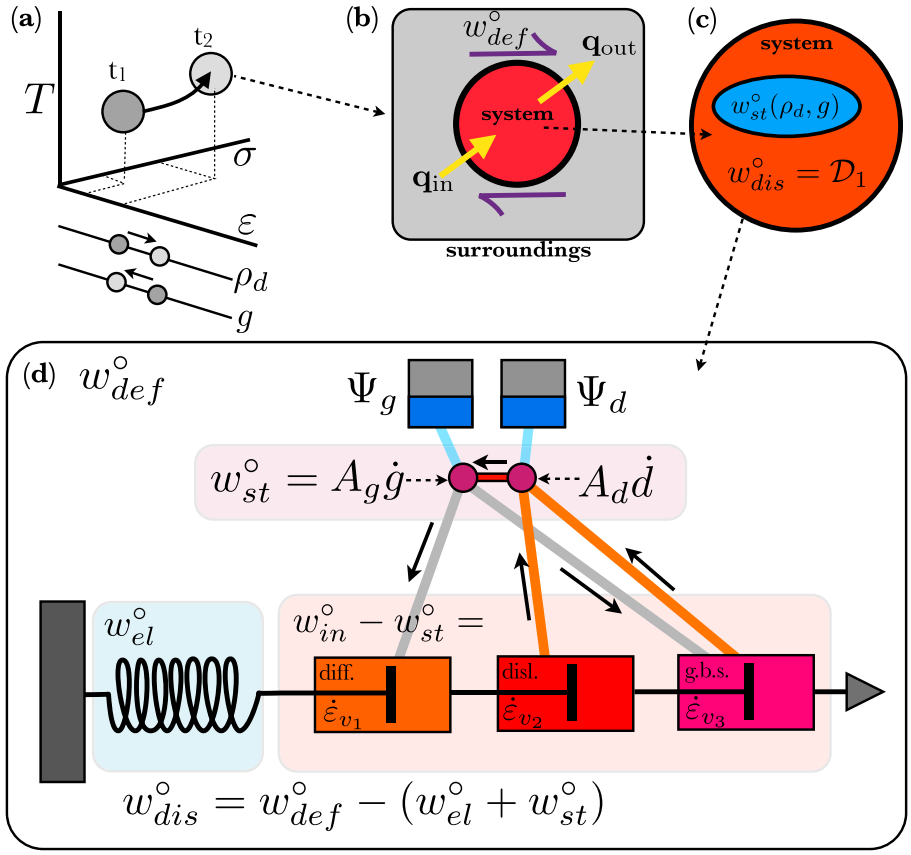

Figure 5. Schematic of the model, with work rates defined in Table 2. (a) Two states in $T - \varepsilon - \sigma - \rho_d - g$ space, connected by a path with irreversible dissipation. The ε is the total strain, but ε_v (not shown) is also needed to describe the state. (b) In the 0-D thermodynamic system of interest here, deformation (work) is applied to a representative elementary volume (orange circle), which is open to heat but not mass. (c) Inside the representative elementary volume, energy can be stored or dissipated. (d) The mechanical model consists of a Maxwell body with three nonlinear creep mechanisms and two microstructural state variables, dislocation density, and grain size. Lines indicate couplings; grey: diffusion creep and grain boundary sliding depend nonlinearly on grain size; orange: dislocation and grain boundary sliding creep both involve dislocation production and motion. Some of those dislocations go into changing the grain size (red line). Any changes in mean dislocation density and grain size involve dissipated energy (purple dots) and a change in the stored energy (blue tanks).

described by a form of Hooke's law: $\sigma = M(\varepsilon - \varepsilon_v)$, where M is the relevant elastic modulus, ε is the total strain, and ε_v is the total viscous strain. We use three creep mechanisms (dashpots in Figure 5d), two of which depend nonlinearly on grain size (diffusion and GBS creep), and two of which depend nonlinearly on stress (GBS and dislocation creep), and all are nonlinear in temperature. Under the quasi-static approximation, the evolution of stress is slow enough that the steady state flow laws are valid for every time interval between two successive states.

We use two microstructural state variables, for the mean dislocation density and mean grain size, such that $\alpha_1 = \rho_d$ and $\alpha_2 = g$, that govern the energy stored in the microstructure (Figure 5d). The dislocation density evolution model is derived in section 3.3; the grain size evolution model is developed in section 3.4, with a significant part to be derived below, in section 4.4.3. The evolution laws are constructed from equations (21), (28), and (31). In Figure 5d, the elements representing energy storage are attached to the viscous dashpots, because they are closely coupled. We will show that small changes in the stored energy yield large changes in the total energy dissipated.

Up front, we make several major simplifications:

1. We consider only scalar values of stress and strain.
2. We assume that mass density is constant, considering a silicate rock that undergoes no reactions, no thermal expansion, or mechanical dilatancy due to cavitation or granular flow, all of which would change the density

Table 4
Empirical Evolution Law Parameters for Dislocation Density and Grain Size

Symbol	Name	Value	Units	Notes
Dislocations				
ρ_d	dislocation density	s.v.	(m^{-2})	Equation (23)
s	stress exponent	1.37	—	Equation (23)
β	dislocation prefactor	1.74E−3	—	Equation (23)
b	Burger's vector	0.5E−9	(m)	Equation (23)
c_1	geometric constant	1.88	—	Equation (24)
μ	shear modulus	50E9	(Pa)	Equation (24)
B^o_{d-}	$\dot{\rho}_{d-}$ rate constant	3.6E−6	(s^{-1} $m^{2(q-1)}$)	Equation (26)
q	exponent	2	—	Equation (26)
Q_{d-}	activation energy	300E3	(J/mol)	Equation (26)
B^o_{d+}	$\dot{\rho}_{d+}$ rate constant	4.9E−4	($s^{-1} m^{-2}$ Pa^{-p})	Equation (27)
p	exponent	$s * q$=2.74	—	Equation (27)
Q_{d+}	$\dot{\rho}_{d+}$ activation energy	300E3	(J/mol)	Equation (27)
Grain size				
g	grain size	s.v.	(m)	Equation (29)
c_2	constant	π	—	Equation (29)
γ	surface energy	1.0	(J/m^2)	Equation (29)
C^o_{gg}	rate constant	2.0E−8	(m^v s^{-1})	Equation (30)
v	exponent	2	—	Equation (30)
Q_{gg}	activation energy	200E3	(J/mol)	Equation (30)
C^o_{sd}	rate constant	4.0E−22[a]	(Pa^{1-a} m^2 s^{-1})	Equation (31)
a	exponent	1.0	—	Equation (31)
Q_{sd}	activation energy	200E3	(J/mol)	Equation (31)
g_{sg}	subgrain size		(m)	Equation (33)
c_{sg}	subgrain piezometer constant	15	—	Equation (33)

Note. Sources are cited near the equations listed in last column. The least constrained parameters are B^o_{d+}, Q_{d+}, C^o_{sd}, a, Q_{sd}. s.v. indicates a state variable.
[a]This value depends on the choice of g_{att}; the value chosen here causes calculated steady state grain sizes to land on roughly on the experimental data in Figures 2 and 7 when g_{att} is the subgrain piezometer.

and thus require mass balance calculations and equations for density. In what follows, we calculate all values per unit volume.

3. Dislocation densities and grain sizes measured in natural and laboratory rocks are nonsingular distributions. The use of only the mean values of properties of the microstructure relies on a fairly strong assumption that the distribution remains self-similar as the mean value evolves.

4.1. Helmholtz Free Energy Potential and State Laws

The volume free energy potential can be constructed in many ways, reflecting the conception of the physical problem and the physical couplings that we choose to consider. Here because the mostly empirical studies of aspects of the problem are separated, as described in section 3, we construct the potential as a sum of the elastic, microstructural, and thermal contributions:

$$\Psi(S_v) = \underbrace{\frac{1}{2}M(\varepsilon - \varepsilon_v)^2}_{\Psi_{el}} + \overbrace{(c_1\mu b^2)\rho_d}^{\Psi_d} + \underbrace{\frac{c_2\gamma}{g}}_{\Psi_g} - \overbrace{\frac{1}{2}C_0\frac{\theta^2}{T_0}}^{\Psi_{th}}, \tag{34}$$

where $\varepsilon_v = \sum_i \varepsilon^{v_i}$ and $\theta = T - T_0$. T_0 is a reference temperature, or in the case of experiments, the initial temperature. The definitions of the internal energies for grain size (surface energy of grain boundaries) and dislocation density (elastic strains around dislocations) were given in section 3 and equations (24) and (29), respectively. Symbols are summarized in Tables 1 and 4.

The *state equations*, derived from the partial derivatives of the free energy potential with respect to each state variable, represent the conjugate variables associated with each state variable. In calculating these derivatives, we illuminate what couplings we are considering in the free energy potential. For example, here we make the approximation to neglect the temperature dependences of μ, b, c_1, c_2, γ, so no thermomechanical coupling terms will be derived from this form of free energy potential; all temperature effects occur in the dissipation potential. The possible effect of temperature on surface energy, $\gamma(T)$, was as discussed in section 3.4. Thus, the state equations read

$$\begin{cases} A_\varepsilon = \frac{\partial \Psi}{\partial \varepsilon} = M(\varepsilon - \varepsilon_v) = \sigma^r \\ A_{v_i} = \frac{\partial \Psi}{\partial \varepsilon_{v_i}} = -\sigma^r \\ A_d = \frac{\partial \Psi}{\partial \rho_d} = c_1 \mu b^2 \\ A_g = \frac{\partial \Psi}{\partial g} = -c_2 \gamma g^{-2} \\ A_{th} = \frac{\partial \Psi}{\partial T} = -s \end{cases} . \tag{35}$$

4.2. Dissipation Potential and Rate Equations

The dissipation pseudopotential Φ is a function of the state variable fluxes $\dot{\mathcal{S}}_v = \{\vec{q}, \dot{\varepsilon}, \dot{\varepsilon}_{v_i}, \dot{\rho}_d, \dot{g}\}$ and parametrized by $\mathcal{S}_v$. We construct a function Φ based on the empirical models discussed in section 3, which are measured in isolation from each other. The additive decomposition of the dissipation potential comes from the hypothesis that the irreversible mechanisms induced by diffusion, dislocation and GBS creep, and grain size and dislocation density changes, can be simply superimposed. So the function is constructed as follows:

$$\Phi(\dot{\mathcal{S}}_v; \mathcal{S}_v) = \sum_i \Phi_{v_i}(\dot{\varepsilon}_{v_i}; \mathcal{S}_v) + \Phi_d(\dot{\rho_d}; \mathcal{S}_v) + \Phi_g(\dot{g}; \mathcal{S}_v) + \Phi_{\text{th}}(\vec{q}; \mathcal{S}_v). \tag{36}$$

In a Maxwell-type viscoelastic model, irreversibility induced by the viscous flow laws (the dashpots) is associated with the viscous strain rates, ε_{v_i}. For the model employed here, the chosen state variables for strain are $\{\varepsilon, \varepsilon_{v_i}\}$. The irreversibility due to deformation alone (not microstructure change, $\dot{g}, \dot{\rho_d}$) is described by ε_v, so there is no dissipation associated with the total strain, that is, $\Phi_{,\dot{\varepsilon}} = 0$, so $\sigma^{\text{ir}} = 0$ and $\sigma = \sigma^r$.

In this model, we switch to the dual pseudopotential, Φ^*, which is the Legendre-Fenchel transform of the pseudopotential. Φ^* is now a function of the set of thermodynamic forces X, which we refer to as $\mathcal{S}_X = \{-\frac{\nabla T}{T}, X_{v_i}, X_\rho, X_g\}$, instead of the fluxes $\dot{\mathcal{S}}_v$, better reflecting the form of all the empirical kinetic models in section 3. However, recall that both forms are strictly equivalent from a physical standpoint. For example, it is convenient to introduce terms in the potential for the steady state flow laws (i.e., $\dot{\varepsilon}_{v_i} = \partial \Phi^*_{v_i} / \partial X_{v_i}$), which are easily identifiable when standard empirical flow laws exist in the literature, (cf. equation (21)). The additive partition of irreversible mechanisms leads us to propose this dual dissipation potential:

$$\Phi^*(\mathcal{S}_X; \mathcal{S}_v) = \sum_i \Phi^*_{v_i}(X_{v_i}; \mathcal{S}_v) + \Phi^*_d(X_d; \mathcal{S}_v) + \Phi^*_g(X_g; \mathcal{S}_v) + \Phi^*_{\text{th}}(X_{\text{th}}; \mathcal{S}_v). \tag{37}$$

The different terms of Φ^* will be successively defined in sections 4.4.1 to 4.4.4.

As already mentioned, in section 2.2, the thermodynamic forces are the partial derivatives of the dissipation pseudopotential with respect to the flux of each state variable. In this model we obtain

$$\begin{cases} X_{\dot{\varepsilon}} = \sigma^{\text{ir}} = \frac{\partial \Phi}{\partial \dot{\varepsilon}} = 0 \\ X_{v_i} = \frac{\partial \Phi}{\partial \dot{\varepsilon}_{v_i}} \\ X_d = \frac{\partial \Phi}{\partial \dot{\rho}_d} \\ X_g = \frac{\partial \Phi}{\partial \dot{g}} \\ X_{\text{th}} = \frac{\partial \Phi}{\partial \vec{q}} \end{cases} . \tag{38}$$

However, as discussed above, we prefer to use the *dual* version of the previous equations, which give us the viscous flow laws and the kinetic equations for dislocation density and grain size:

$$\begin{cases} \dot{\varepsilon}_{v_i} = \frac{\partial \Phi^*}{\partial X_{v_i}} \\ \dot{\rho}_d = \frac{\partial \Phi^*}{\partial X_d} \\ \dot{g} = \frac{\partial \Phi^*}{\partial X_g} \\ \vec{q} = \frac{\partial \Phi^*}{\partial X_{\text{th}}} \end{cases} . \tag{39}$$

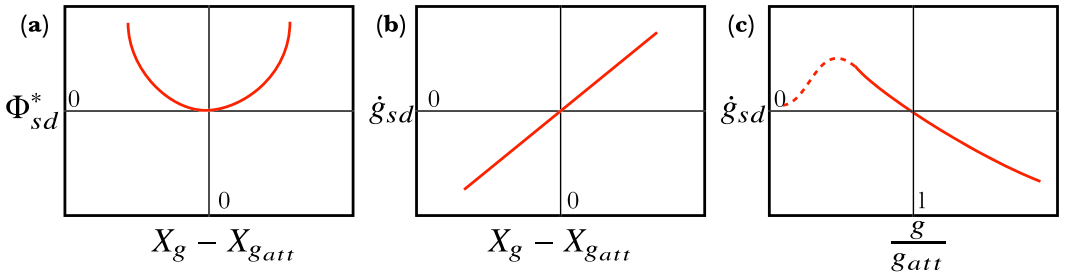

Figure 6. (a) The dissipation potential for stress-driven grain size evolution, Φ^*_{sd}, is a convex function centered on the difference between the thermodynamic driving force component X_g and a reference $X_{g_{att}}$. (b) The derivative of this function with respect to X_g gives $\dot{g}_{sd}$, which is a positively sloping line. (c) When this rate is recast in terms of the grain size (relative to the attractor grain size, g_{att}, it shows that the grain size will decrease when $g > g_{att}$; the stress-driven grain growth can occur when $g < g_{att}$, but the effect is limited by the presence of σ in the function, so the effect be mitigated at low stress (implied by the dashed line).

Note that the total strain rate $\dot{\varepsilon}$ cannot be derived from the dissipation potential since $\sigma^{ir} = 0$. This is consistent because the total strain is not used to describe the irreversible mechanisms. The strain will be related to the other state variables through the state laws. Regarding the other rate equations, it is clear now how the empirical laws proposed in section 3 fit into the GSM. Below, we elucidate the different thermodynamic forces.

4.3. Relationships Between Thermodynamic Forces and Conjugate Variables

As discussed above in section 2, the intrinsic dissipation was defined and written as the product of the thermodynamic forces and fluxes associated with state variables. The intrinsic dissipation is written as

$$\mathcal{D}_1 = \sum_i X_{\dot{\varepsilon}_{v_i}} \dot{\varepsilon}_{v_i} + X_g \dot{g} + X_d \dot{\rho}_d \geq 0 \tag{40}$$

Following the Clausius-Duhem inequality (cf. equation (3)), the intrinsic dissipation can also be written as

$$\mathcal{D}_1 = \left(\sigma - A_\varepsilon\right) \dot{\varepsilon} - \sum_i A_{v_i} \dot{\varepsilon}_{v_i} - A_g \dot{g} - A_d \dot{\rho}_d \geq 0, \tag{41}$$

By inspection of equations (40) and (41), and noting that both expression of $\mathcal{D}_1$ must be identical whatever the thermodynamic process, we obtain

$$\begin{cases} \sigma = A_\varepsilon = \sigma^r \\ X_{v_i} + A_{v_i} = 0 \\ X_d + A_d = 0 \\ X_g + A_g = 0 \end{cases}. \tag{42}$$

4.4. Construction of the Dissipation Potential

In the following, we consider the different irreversible mechanisms accompanying the deformation process.

4.4.1. Nonlinear Viscous Creep

Regarding the viscous flow laws introduced in equation (3.2), we propose a contribution to the dissipation potential of the following form

$$\Phi^*_{v_i}(X_{v_i}; \mathcal{S}_v) = \frac{1}{n_i + 1} C_{v_i}(T) g^{-m_i} |X_{v_i}|^{n_i + 1}, \tag{43}$$

where $X_{v_i} = \sigma$ and, according to equations (35) and (42), $C_{v_i}(T)$, $i \in \{1, 2, 3\}$ are functions of temperature for each of the three flow laws. Note that the values of the thermodynamic force associated with each of the viscous strain rates are by construction (i.e., dashpots in series) equal to σ, which is itself equal to σ^r.

4.4.2. Stress-Driven Dislocation Density Evolution

To calculate the dissipation potential, recall that $\dot{\rho}_d = \frac{\partial \Phi^*}{\partial X_d}$. Because Ψ_d is linear in ρ_d ($\Psi_d = c_2 \mu b^2 \rho_d$), X_d is composed of only constants ($-c_2 \mu b^2$). Since we cannot write ρ_d in terms of X_d, the integration of the empirical equation for dislocation density evolution (equation (28)) is simply

$$\Phi^*_d(X_d; \mathcal{S}_v) = \left(B_{d^+}(T) \sigma^p - B_{d^-}(T) \rho_d^q\right) X_d, \tag{44}$$

We note that σ here is interpreted as a parameter in the dissipation potential, as it is not a state variable but is a function of them, $\sigma = M(\varepsilon - \varepsilon_v)$. For lack of more empirical insight, we assume that the thermodynamic force for dislocation density evolution, X_d, only affects Φ^*_d. Because of the smooth transitions among mobile and forest dislocations, subgrains and grain boundaries, we expect that these discrete evolution laws and dissipation potential terms are artificially decoupled.

4.4.3. Grain Size Evolution

As discussed in section 3.4, the grain size evolution equation has additive (serial) terms for static growth and stress-driven change. These terms can be separated in deriving the dissipation potential, as $\Phi^*_g(X_g; \mathcal{S}_v) = \Phi^*_{gg} + \Phi^*_{sd}$. To obtain Φ^*_{gg}, substituting in $X_g = c_2\gamma/g^2$ (recalling that $X = -A$ with equations (35) and (39) into equation (30) yields

$$\Phi^*_{gg}(X_g; \mathcal{S}_v) = \frac{C_{gg}(T)}{\gamma}(c_2\gamma)^{\frac{v-1}{2}}\frac{2}{v+1}X_g^{\frac{v+1}{2}}. \tag{45}$$

The stress-driven grain size evolution term (growth and reduction associated with deformation) is more hypothetical and less empirically constrained than other aspects of this problem (section 3.4). Therefore, unlike the above terms, we derive an evolution law from a potential. Ideally, we want to quantify the notion of a distance from steady state that can be modulated by a given process. An approach to this problem is illustrated qualitatively in Figure 6. In the context of the GSM, we seek a simple quadratic (convex) form in X_g. Near steady state it is reasonable to hypothesize that the driving force is the difference between the present state and the steady state, with the notion of a steady state determined by a known function of an *attractor* grain size g_{att}, as illustrated in Figure 6a:

$$\Phi^*_{sd}(X_g; \mathcal{S}_v) = \frac{C_{sd}(T)}{2}\sigma^a\left(X_g - X_{g_{att}}\right)^2. \tag{46}$$

The stress-driven grain size evolution rate $\dot{g}_{sd}$ is the partial derivative of this piece of the dissipation potential with respect to the thermodynamic force driving grain size evolution X_g, which is linear with distance from steady state:

$$\dot{g}_{sd} = \frac{\partial\Phi^*_{sd}}{\partial X_g} = C_{sd}(T)\sigma^a\left(X_g - X_{g_{att}}\right), \tag{47}$$

as shown in Figure 6b. When we substitute in X_g, we get

$$\dot{g}_{sd} = C_{sd}(T)\sigma^a\left(\frac{c_2\gamma}{g^2} - \frac{c_2\gamma}{g^2_{att}}\right). \tag{48}$$

This function gives a nonlinear function of grain size, as illustrated in Figure 6c, when plotted against g/g_{att}.

In the present form of the model, this equation represents a single process, subgrain rotation recrystallization, that will have single values of the constants, and a single function for g_{att}. As an initial hypothesis to be tested against experimental data, we propose that function is the subgrain size piezometer, such that $g_{att} = g_{sg}$ and allow the rate to also be functions of stress ($\dot{g}_{sd} \propto \sigma^a$) and temperature, assuming that $C_{sd}(T) = C^0_{sd}\exp(-Q_{sd}/RT)$. As shown in Figure 6c, grain size will decrease when $g > g_{att}$, and increase when $g < g_{att}$. When stress is very low, the rate is very small, so the stress-driven grain growth behavior is self-limited (dashed line in Figure 6), as we show in section 5.3. The latter effect may still be exaggerated, but we do not yet have the experimental data to constrain any asymmetry in the function for Φ^*_{sd} that would be required. Importantly, g_{att} is a function of the dislocation density, which is a function of stress and temperature, strongly coupling the evolution equations ($[\dot{\rho}_d \rightarrow \dot{g}_{sg} \rightarrow \dot{g}]$). Therefore, the attractor can be a moving target during the evolution of the system and the coefficients C determine how well g can keep up with g_{att}.

4.4.4. Thermal Dissipation Potential and Fourier's Law

The main goal of the thermal dissipation potential $\Phi^*_{th}(X_{th}; \mathcal{S}_v)$ is to include in the model heat diffusion mechanisms, generally described by Fourier's law. By construction, we must have $\vec{q} = \frac{\partial\Phi^*}{\partial X_{th}} = -k\nabla T$, where k is the isotropic heat conduction coefficient. We then propose the following expression for Φ^*_{th}:

$$\Phi^*_{th} = \frac{kT}{2}X^2_{th}. \tag{49}$$

As seen in equation(10) the heat diffusion equation is a partial differential equation involving time and space variables. For the sake of simplicity we will consider in the following a simplified version of this equation leading to an ordinary differential equation (ODE) in time (Chrysochoos & Louche, 2000). Under several conditions (e.g., homogeneity of the heat source field and linearity of the thermal boundary conditions), the Laplacian term reflecting heat conduction can be replaced by a simple linear term in temperature variation θ. The heat diffusion can then be simplified as

$$\rho c\left(\dot{\theta}+\frac{\theta}{\tau_{\text{th}}}\right)=\mathcal{D}_1, \tag{50}$$

more usefully viewed as $\dot{\theta}=\frac{\mathcal{D}_1}{\rho c}-\frac{\theta}{\tau_{\text{th}}}$, and where τ_{th} is a time constant characterizing the local heat losses. Below we will consider three cases for thermal conditions: isothermal ($\tau_{\text{th}}\rightarrow 1$), adiabatic ($\tau_{\text{th}}\rightarrow\infty$) and an intermediate case where there is a finite τ_{th} based on experimental results, described in Appendix B2.

4.4.5. Concluding Comments on the Dissipation Potential

In the previous sections 4.4.1 to 4.4.4 we defined step by step the different contributions constituting of the dissipation potential. In the GSM framework, we have shown that a sufficient condition to get constitutive equations in agreement with the second principle of thermodynamics is to use a dissipation potential $\Phi^*(\mathcal{S}_X)$ having the following properties:

- Convexity of $\Phi^*(\mathcal{S}_X)$
- Positivity of $\Phi^*(\mathcal{S}_X)$
- $\Phi^*(\mathcal{S}_X=\{\mathbf{0},\mathbf{0},\mathbf{0}\})=0$

where $\mathcal{S}_X$ symbolizes the set of thermodynamic forces that drive dissipation, as described in section 4.2. Even if the properties [i] and [iii] of the potential $\Phi^*(\mathcal{S}_X)$ proposed above are verified, its positivity [ii] still has to be checked a posteriori. Indeed, $\Phi^*(\mathcal{S}_X)$ depends not only on the $\mathcal{S}_X$ values but also on the different material constants present in the model. As will be demonstrated in section 5, the total dissipation is found to be positive for all thermodynamic processes studied here, even if, in a case where grain size reduction is causing a storage of energy, the energy storage rate is significantly less than the viscous dissipation due to creep mechanisms.

4.5. Work, Energy, and the Taylor-Quinney Coefficient

As discussed in section 2.4, the GSM formalism enables the tracking of stored and dissipated energy during deformation. We calculate the internal dissipation $\mathcal{D}_1$ during the computation to determine the temperature change and other aspects of the energy budget in postprocessing. In particular, we are interested in comparing the ratio of stored to dissipated work rate F_{w° and the λ_{AE}, discussed in section 1.1. Recall that $F_{w^\circ}=\frac{w_s^\circ}{w_{\text{in}}^\circ}$. The stored work rate w_s° (the fraction of mechanical energy rate that goes into changing the microstructure) is $w_s^\circ=A_d\dot{\rho}_d+A_g\dot{g}$, and the inelastic work rate $w_{\text{in}}^\circ=\sigma(\sum_i\dot{\varepsilon}_{v_i})$, such that

$$F_{w^\circ}=\frac{w_s^\circ}{w_{\text{in}}^\circ}=\frac{A_d\dot{\rho}_d+A_g\dot{g}}{\sigma(\sum_i\dot{\varepsilon}_{v_i})}=\frac{-\left(X_d\dot{\rho}_d+X_g\dot{g}\right)}{\sigma(\sum_i\dot{\varepsilon}_{v_i})}. \tag{51}$$

Thus, because $A_d=c_1\mu b$ and $A_g=-c_2\gamma g^{-2}$, $F_{w^\circ}>0$ when energy is being increasingly stored in the microstructure, and $F_{w^\circ}<0$ when energy is being dumped from the microstructure and turning into heat. Also, when the microstructure is in steady state ($\dot{\rho}_d,\dot{g}=0$), $F_{w^\circ}=0$. Therefore, since λ_{AE} is intended to describe partitioning at steady state, $F_{w^\circ}\neq\lambda_{\text{AE}}$.

Though similar in its role as a ratio of energy dissipation and storage rates, λ_{AE} must have a different definition. Austin and Evans (2007, 2009) define the internal dissipation (using our equivalent notation) as

$$\mathcal{D}_1=(1-R_{\text{disl}})\sigma\dot{\varepsilon}_v+(1-\lambda_{\text{AE}})R_{\text{disl}}\sigma\dot{\varepsilon}_v, \tag{52}$$

where the ratio of dislocation creep rate (disl) to total creep rate $R_{\text{disl}}=\frac{w_{\text{disl}}^\circ}{w_{\text{in}}^\circ}=\frac{\dot{\varepsilon}_{\text{Disl}}}{\dot{\varepsilon}_v}$ (which is β in their terminology). Because we are considering flow laws for two dislocation-based processes, we include GBS along with dislocation creep, such that $\dot{\varepsilon}_{\text{Disl}}=\dot{\varepsilon}_{\text{gbs}}+\dot{\varepsilon}_{\text{disl}}$. The λ_{AE} is specifically the fraction of energy that would otherwise be dissipated as dislocation creep that is instead diverted into changing the microstructure (through motion

of dislocations into subgrain walls and grain boundaries) and thus the stored energy in the microstructure. Furthermore, λ_{AE} cannot equal zero at steady state, because the grains would grow by the static grain growth term, and dislocations would anneal, so the microstructure would not be in steady state. Therefore, we define λ_{AE} as follows: because $A_d\dot{\rho}_d = A_d(\dot{\rho}_d^+ + \dot{\rho}_d^-)$ and $A_g\dot{g} = A_g(\dot{g}^{sd} + \dot{g}^+)$, we propose that only the stress-driven terms contribute to λ_{AE}, with the annealing terms removed, such that

$$\lambda_{AE} = \frac{A_d\dot{\rho}_d^+ + A_g\dot{g}^{sd}}{\sigma\left(\dot{\varepsilon}_{gbs} + \dot{\varepsilon}_{disl}\right)}. \tag{53}$$

Thus, at steady state, $\lambda_{AE} > 0$. Note that this equation is identical to solving equation (22) in Austin and Evans (2009) for λ (assuming $\dot{\rho}_d = 0$). This value will be plotted in the following results. Austin and Evans (2007, 2009) chose a fixed value of $\lambda_{AE} = 0.1$ based on studies on metals, citing energy partitioning measured by Chrysochoos et al. (1989).

5. Solutions and Results

Of the many possible variations of the model developed above, the system of coupled, nonlinear differential equations to be solved is constructed from the Maxwell-type mechanical model, the flow laws and the evolution laws for ρ_d and g (equations (21), (28), and (31)). The dislocation density evolution model is derived in section 3.3 and Appendix A; the grain size evolution model is developed in sections 3.4 and 4.4.3. The dissipation $\mathcal{D}_1$ (equation (41)), which enters into the temperature evolution (equation (50)), and the equation of state for subgrain size g_{sg} as the attractor g_{att} provide closure to the system:

$$\begin{cases} \dot{\sigma} = M(\dot{\varepsilon} - \dot{\varepsilon}_v) & \text{(54a)} \\ \dot{\varepsilon}_v = \sum_i (C_{v_i}(T)\sigma^{n_i} g^{-m_i}) & \text{(54b)} \\ \dot{\rho}_d = B_{d^+}(T)\sigma^p - B_{d^-}(T)\rho_d^q & \text{(54c)} \\ \dot{g} = C_{sd}(T)\sigma^a\left(\frac{c_g}{g^2} - \frac{c_g}{g_{att}^2}\right) + C_{gg}(T)g^{1-v}/v & \text{(54d)} \\ \dot{\theta} = \frac{\mathcal{D}_1}{\rho c} - \frac{\theta}{\tau_{th}} & \text{(54e)} \end{cases}$$

With the following closure equations

$$g_{att} = g_{sg} = \frac{c_{sg}}{\sqrt{\rho_d}} \tag{55}$$

$$\mathcal{D}_1 = \sigma\left(\sum \dot{\varepsilon}_{v_i}\right) - A_g\dot{g} - A_d\dot{\rho}_d. \tag{56}$$

Recall that the thermal terms (C_{v_i}, B, C) are all of the form $X(T) = X^0\exp(-Q/RT)$, neglecting pressure dependences. In the solutions presented in this paper, we integrate the above equations under strain-controlled conditions, $\dot{\varepsilon} = \dot{\varepsilon}_{control}$, leaving stress-controlled conditions for future work. In postprocessing, we calculate the various work rates and λ_{AE} (equation (53)).

In the following, we first present steady state solutions fit to experimental data, and then provide time-dependent solutions with the intent to show the general behavior of the system of ODEs (i.e., zero spatial dimensions), followed by an application to analysis of data from torsional deformation experiments. For strain-controlled conditions (equation (54)), we first present results from two runs differing only in their thermal time constants τ_{th} = [1E2, 1E4], approximating isothermal and adiabatic conditions, respectively. We then present the results for a suite of numerical tests varying strain rate and temperature, $[\dot{\varepsilon}, T_0]$, to look at the predictions for steady state grain size, also for isothermal and adiabatic conditions. We then solve these equations in a geometry approximating torsional deformation experiments, to illustrate how experimental data will constrain unknown constants in the evolution equations for dislocation density and grain size.

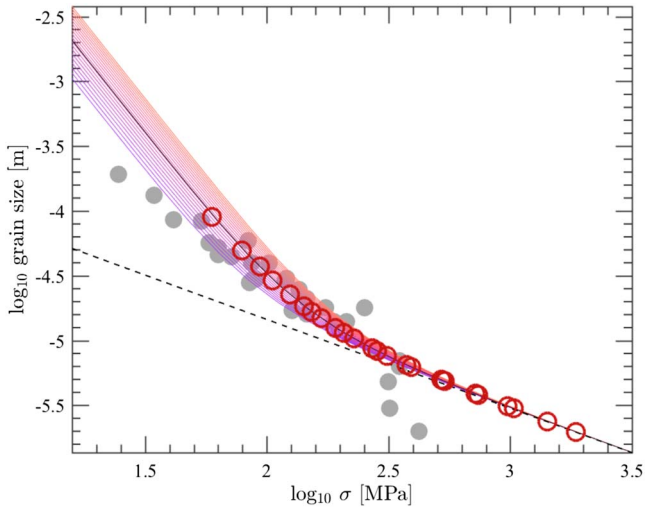

Figure 7. Steady state solutions (equation (57)) overlying the experimental data from Figure 2 (gray dots) and the solutions from the ordinary differential equations (red hollow dots) presented in subsequent figures. The solid black line is the steady state solution assuming $Q_{gg} = Q_{sd}$, as in the ordinary differential equation calculations. The colored lines show the steady state solutions assuming (as an arbitrary example) that Q_{gg} is 20% greater than Q_{sd}; redder lines reflect higher temperature. The black dashed line is the Toriumi subgrain piezometer, $g_{att} = g_{sg}(\sigma)$.

5.1. Steady State Solutions

In principle, a steady state (for microstructure and mechanical properties) is possible only if the heat loss is nonzero, that is, a nonadiabatic process. In the present model, this is the case when τ_{th} is constant and short compared to the experiment duration. The steady state grain size can be approximated by assuming that the dislocation density is at its steady state, determined by the piezometer (section 3.3 and equation (55), such that the attractor grain size g_{att} is a function of stress at steady state. The grain size evolution equation can be set to zero such that its static grain growth and stress-driven terms are equal and solved for grain size (also assuming that $v_{gg} = 2$), taking the positive solution of the quadratic:

$$g_{ss} = \frac{C_{gg}(T)g_{att} + \sqrt{C_{gg}(T)^2 g_{att}^2 + 16C_{sd}(T)^2\sigma^{2a}c_g^2}}{4C_{sd}\sigma^a c_g}. \quad (57)$$

The results, shown in Figure 7, demonstrate the steady state solutions closely fit the g_{att} line above a critical level of stress. Below that level, static grain growth pushes the steady state grain size above the attractor line, referred to as the grain growth-dominated regime. This result also implies that the grain size will never be smaller than the subgrain size (g_{att}), which is physically sensible. The steady state predictions fits very well with the numerical solutions (open red circles) and falls within range of the experimental data (gray dots) from Figure 2. If $Q_{gg} \neq Q_{sd}$, there is a temperature dependence to the steady state at stresses in the grain growth-dominated regime, but not above. These lines were calculated with $Q_{gg} = 1.2Q_{sd}$, resulting in higher temperatures yielding higher steady state grain size in the growth-dominated regime. In the time-dependent solutions, we assume that $Q_{gg} = Q_{sd}$ and can fit the experimental data fairly well adjusting C_{sd}, as shown in Figure 2. The

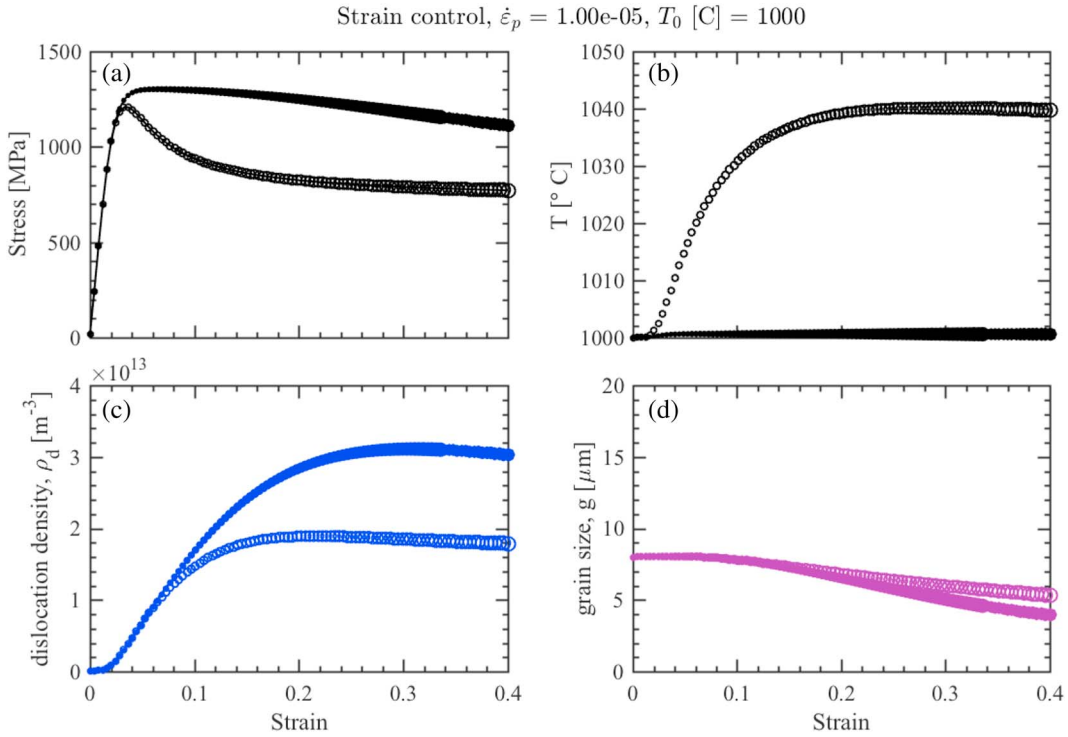

Figure 8. Results for isothermal (solid dots) and adiabatic (hollow circles) conditions, all as a function of strain. (a) Stress, (b) temperature, (c) dislocation density, ρ_d, and (d) grain size, g.

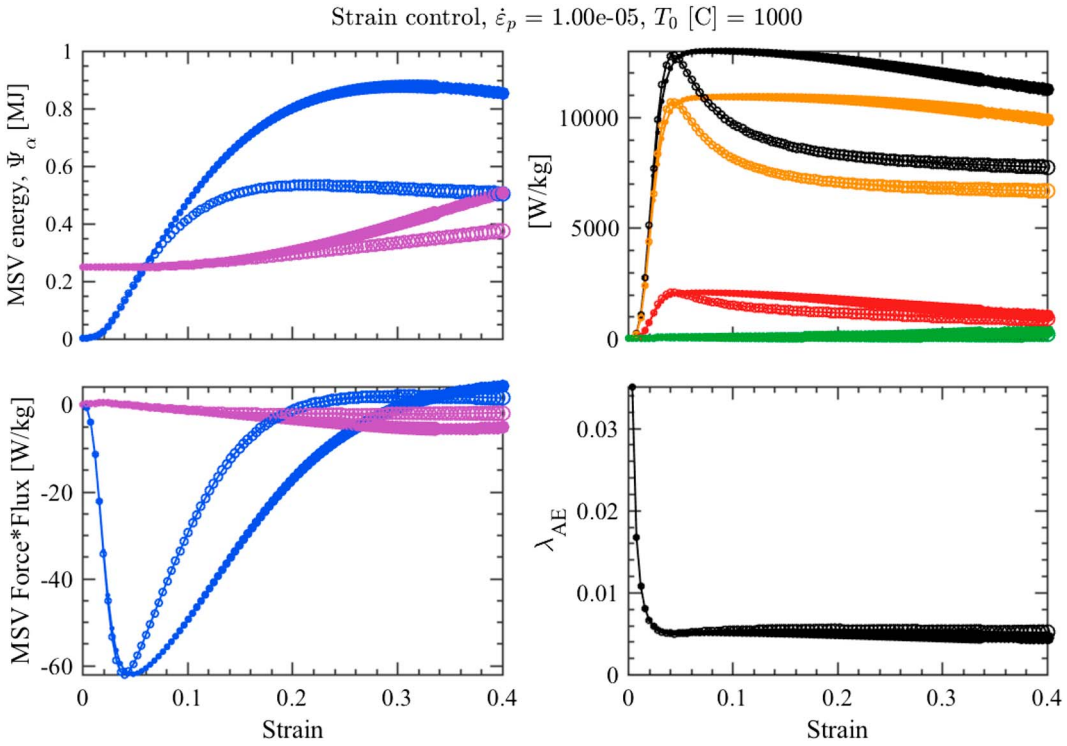

Figure 9. Results for isothermal (solid dots) and adiabatic (hollow circles) conditions, all as a function of strain. (a) Free energy stored in microstructural state variables (MSV), dislocation density, ρ_d (blue) and grain size, g (purple). (b) Viscous dissipations, black = total dissipation $\mathcal{D}_1$, others are dissipation contributions from each creep mechanism (green = diffusion creep; red = dislocation creep; orange = dislocation-accommodated grain boundary sliding creep). (c) Dissipation contributions from changing g (purple) and ρ_d (blue). (d) λ_{AE}, energy partitioning coefficient.

agreement between the steady state and numerical solutions is demonstrated. In the following sections, we look at time-dependent solutions for further insight into the physics.

5.2. Single-Run, Strain-Controlled Experiment

We present the solutions to equations (54)–(56) in Figure 8, comparing an isothermal run (a thermal time constant of $\tau_{th} = 100$ s), with an approximately adiabatic run ($\tau_{th} = 1E4$ s) The calculation is run to a small strain of $\varepsilon_f = 0.4$, at an initial temperature of 1000 °C. Under constant strain rate conditions, the stress increases rapidly until it begins to yield, reaches a peak, and then decreases, for both isothermal and adiabatic runs. The isothermal run reaches steady state at about $\varepsilon = 0.2$; the adiabatic run does not reach steady state because temperature is continually increasing, as shown in Figure 8b. The thermal condition is important; temperature increases by >40 °C in the adiabatic case by $\varepsilon = 0.4$. In the second row of Figure 8, we show the evolution of the microstructural state variables. Dislocation density increases quickly as the stress rises (Figure 8c), while grain size gradually decreases. For both, the adiabatic case leads to more gentle microstructural change because of the higher temperatures and thus lower stresses. In a constant stress calculation, not performed here, the feedbacks would be more intense.

Next, we illustrate aspects of the energetics for the same runs. In Figure 9a, the energies stored in ρ_d and g increase and then plateau, but neither reach equality (as would be expected for the Twiss piezometer model). In Figure 9b, we plot the total intrinsic dissipation $\mathcal{D}_1$ (equation (41)), as well as that due to each creep mechanism. Those creep mechanisms are summing to almost the total value, whereas the dissipations associated with changing the microstructural state variables, ρ_d and g, are much smaller, as shown in Figure 9c. While GBS clearly dominates in this case, the temperature increase in the adiabatic case causes a decrease in all the more nonlinearly stress-dependent mechanisms, that is, a relative increase in diffusion creep. The dissipation rates due to microstructural change (Figure 9c) show negative values of the microstructural contribution to the dissipation, indicating that energy is initially being stored, as ρ_d increases or g decreases. These dissipation rates are very small relative to the creep contributions, so even though they are negative early in the evolution as energy is stored in the dislocation density, the total remains positive. Finally, we plot λ_{AE} (equation (53)

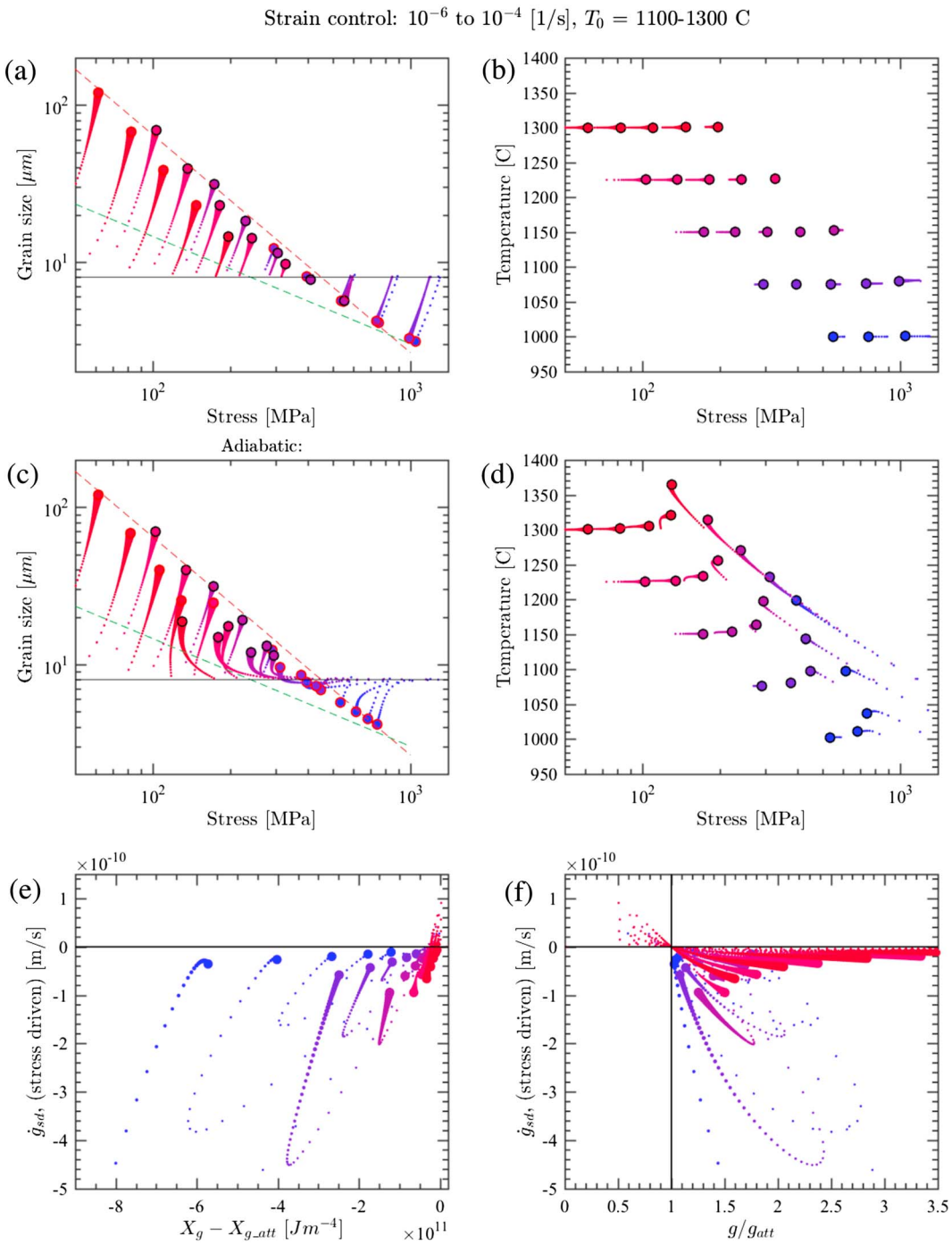

Figure 10. Suites of runs represented in stress-grain size (a, c) and stress-temperature spaces (b, d). The top row is for nearly isothermal runs (τ_{th} = 100 s), and the bottom row is nearly adiabatic (τ_{th} = 1E4 s). The dashed red dashed line in (b) and (d) is the Twiss piezometer; the dashed green line is the Toriumi subgrain piezometer, which is the g_{att} in this model. Note that the grain size initially migrates toward g_{att}, but grain growth drives grain sizes toward the Twiss attractor; the steady state value is controlled by varying C^0_{sd}. The initial grain size is 8 μm. Dot radius increases with time, or strain, up to a final strain of 3.0. The bottom two panels (e, f) show the stress-driven grain size evolution $\dot{g}_{sd}$ for each run (e) as a function of X, and (f) as a function of g/g_{att}, as illustrated qualitatively in Figure 6. Redder colors are higher temperatures. Note that $\dot{g}_{sd} > 0$ only for short times in the initial stages of higher-temperature runs. Lower-temperature runs experience more severe reduction.

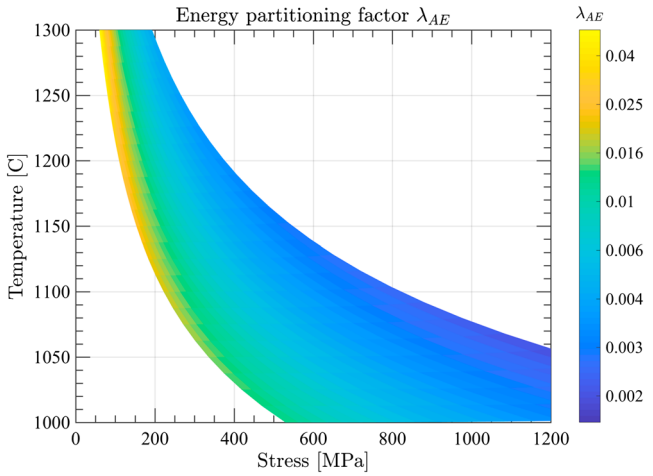

Figure 11. The λ_{AE} versus stress and temperature. The partitioning coefficient is a function of temperature and grain size but may or may not be a state function. Thus, during an evolution, a material will change its partitioning, but that ratio should migrate on this surface with additional dimensions for ρ_d and g.

and Figure 9d) from the values shown in Figures 9b and 9c. In this run, λ_{AE} is always positive, starts large as dislocation density increases as stress is loaded into the material, and then decreases toward about 0.05, but does not reach 0.

5.3. Multiple Runs, Varying $[\dot{\varepsilon}_p, T_0]$

Here we demonstrate the behavior of the solutions in a more compact way, for two sets (isothermal and adiabatic) of 25 runs varying $\dot{\varepsilon}_p$ and T_0, plotting σ versus g and σ versus T in Figure 10. The top row shows the isothermal runs; the *tadpole* tails show the evolution in time through each space, with dot size increasing with time or strain. Isothermal runs take fairly straight paths from the peak stress and initial grain size to the final stress and grain size. Runs at higher stress reach steady state at a smaller grain size, while the lower stress (slower and higher temperature) runs experience net grain growth. In panels (a) and (c), the green dashed line is the Toriumi subgrain size piezometer, $g_{att} = g_{sd}(\sigma)$. While there is some motion toward g_{att}, grain growth is clearly important and leads to a steady state value that is very close to the Twiss piezometer as modified by Hirth and Kohlstedt (2015; red dashed line, same as in Figure 2). Note that the Twiss line corresponds to a certain value of C_{sd}, chosen to illustrate this point. In the adiabatic cases, the final grain sizes look fairly similar as the isothermal cases, but the paths taken to get there are very different, decreasing in stress while increasing in grain size and temperature making more circuitous tadpole tails than the isothermal cases, with more scatter in the final values (that are not at steady state). In the right panel plots of $T - \sigma$ space, the isothermal cases are self-evident. Shear heating appears clearly in the lower right panel, occurring more strongly for the higher strain rate runs, at a given temperature and more dramatically for the lower temperature runs.

Associated with each of these runs, we plot $\dot{g}_{sd}$ in Figures 10e and 10f. The higher stress, lower-temperature runs are dominated by stress-driven reduction, while the lower stress, higher-temperature run appear to have some stress-driven grain growth occurring. However, it is clear that this occurs only at low strain during initial

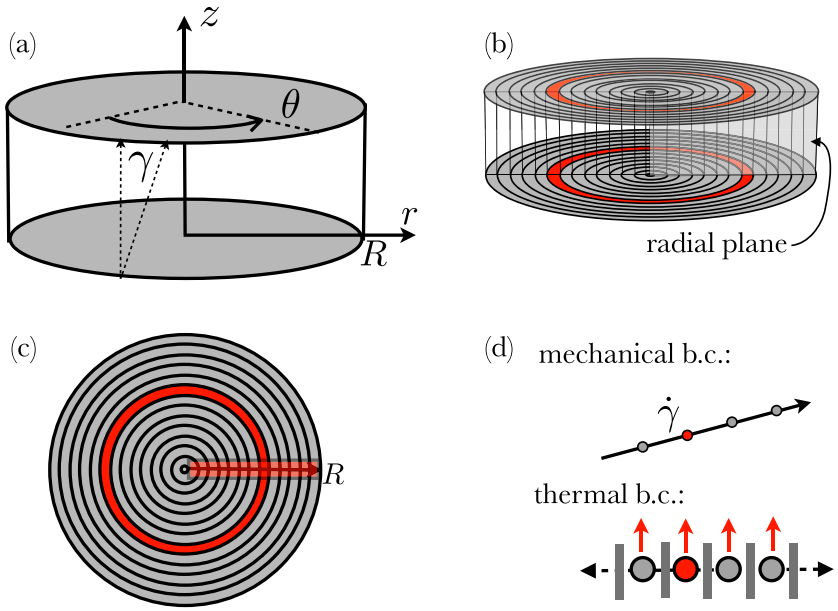

Figure 12. Reduced analysis of torsion experiments. (a) Sample geometry. (b) Each ordinary differential equation model run represents a concentric annulus, described in Appendix B. (c) Top view of annuli. (d) A row of 0-D models with boundary conditions on strain rate, and illustrating the limitation that heat can only diffuse out of each ring, not from one ring to another, in this simple form of the model.

transient creep (where the dot size represents the evolution of the run). We leave further assessment of the relative contributions of static and stress-driven grain growth to analysis of torsion experiments.

We also plot λ_{AE} (at the final strain step for each run) in Figure 11. Overall, for the range of conditions explored, $0.025 < \lambda_{AE} < 0.35$. It is clearly a function of T and σ but also g and ρ_d (not shown); that is, $\lambda_{AE}(\mathcal{S}_v)$, but is not a state function as it is derived from w°_{st}. The value of $\lambda_{AE} = 0.1$ used by Austin and Evans (2007, 2009) lies in the middle of the range. There are clear systematics to the values of λ_{AE}: the surface makes a clear cuspate form, such that at a given temperature, λ_{AE} decreases with increasing stress and similarly for fixed stress and increasing temperature. In other words, creep dissipation increases faster than the storage of energy, reflecting an increase in the diffusion creep component with decreasing grain size (at higher stresses).

5.4. Application to Torsion Experiments

As discussed above, one aim of this model is to provide an integrative thermodynamic framework for the analysis of experiments. Torsion experiments at high temperature and pressure provide both the ability to deform to large strains and also contain a gradient of increasing strain from center to edge. This analysis is a reduced time-dependent simulation of a torsion experiment, as illustrated in Figure 12. The torsion sample is treated as a set of concentric cylindrical rings or annuli; the set of rings is subjected to a constant twist rate, such that each is sheared at a rate that is linearly proportional to their distance from the center, as $\dot{\gamma}_i = \frac{r_i}{R}\dot{\gamma}_{max}$. Each ring is considered to be homogeneous in the z direction (no strain localization) and in the θ direction, such that each ring can be described by a single ODE calculation. In Appendix equation (A1), we demonstrate that this setup does not violate mechanical equilibrium for idealized torsional deformation. We also articulate the relationships between the strain and stress components in torsion and the 0-D models. The major limitation of this approach may be in the thermal behavior; in the present model, heat cannot diffuse between 0-D models, so we cannot assess the extent to which heat generated by mechanical dissipation inside the sample affects the behavior. We use a thermal time constant $\tau_{th} = 700$ s, a value that comes from the temperature-time curves measured after the furnace is switched off, discussed further in equation (A3).

We compare to the data from one torsion experiment performed at the University of Minnesota (D. King et al., personal communication, April 27, 2013) at 1250 °C, with a twist rate of 1.7E−4 radians/s (at the outer edge, $\dot{\gamma} = 1.7\text{E}{-4}\ \text{s}^{-1}$, sample radius 4.8 mm), with initial grain size $g_0 = 8$ μm. Torque was measured on an internal load cell, and the mean grain size was measured by a linear intercept method. While there are many uncertainties in the parameter choices, the primary unknowns in our view, at present, are C^o_{sd}, a, Q_{sd}, as discussed in section 2 and Table 4. For this illustrative example, we sought values of C^o_{sd} and a that are consistent with the grain size profile and torque-time curve.

The results, illustrated in Figures 13, show that we are able to match the grain size profile and the torque-time curve fairly well, for the chosen values of unknowns. In the T-radius plot (Figure 13d), there is little change in T for the experimental $\tau_{th} = 700$ s; thus, it is not likely that at 1250 °C there is significant internal heating. We need observations of dislocation density to constrain further, the degree of *disequilibrium* between the dislocation density and the mean grain size. Note that these values will depend on the choice of g_{att}; these values are not intended to be used for extrapolation to natural conditions until we can perform a systematic analysis over multiple experiments.

In future work, we will have dislocation density profiles and experiments performed at different temperatures and multiple twist rates. There now exists an efficient means to measure dislocation density across such a large sample (Wallis et al., 2016); this technique will be used in the future analysis of torsion experiments. We will perform robust inversions for unknown parameters and explore different hypotheses for g_{att}. The constants in the evolution laws (if the evolution laws are meaningful) should not depend on the mechanical or thermal boundary conditions. This independence can be tested when the appropriate experiments can be compared, including strain-controlled and stress-controlled experiments at different conditions.

6. Questions and Discussion

The GSM thermodynamic formalism is used to build a framework for the analysis of dislocation density and grain size evolution in experiments, toward a better understanding of microstructure evolution and transient creep, as well as the characterization of the steady state. This formalism introduces the dissipation pseudopotential Φ, which provides far more freedom in the form of the evolution laws than the linear TIP (i.e., for grain size and dislocation density in this study). In the analysis of experimental data, many forms of

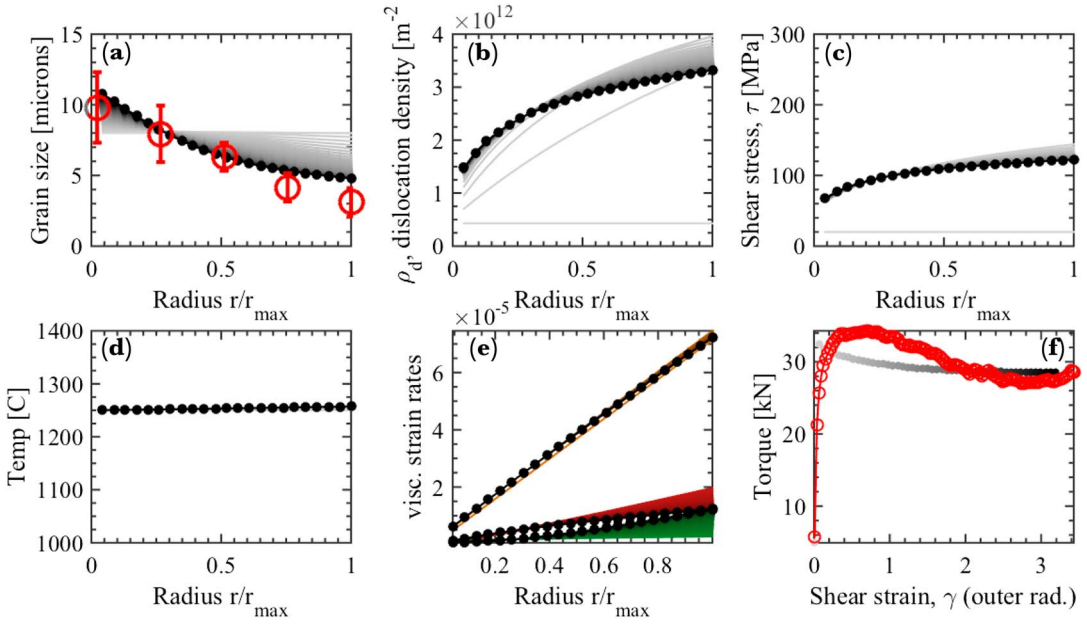

Figure 13. Application of analysis to interpretation of data from torsion experiments. All plots except lower right plot show data as a function of radius, center to edge, with time indicated by gray values increasing to black. (a) Grain size. The values of g decrease from center to edge, because the differential stress increases from center to edge. Data from one experiment described in the text are shown in red dots. (b) Dislocation density increases from center to edge, but at the outer edge does reach a peak and then decreases, as stress drops (due to grain size reduction). (c) The shear stress increases from center to edge but remains fairly flat, without a dramatic decrease. (d) Temperature. With such a short thermal time constant of τ_{th} = 700 s, there is negligible dissipative heating. Note that thermal diffusion is not being calculated along the radius. (e) Strain rates of each creep mechanism. Colors are as in Figure 9. The whole sample is in grain boundary sliding creep. (f) Torque as a function of shear strain at the outer radius. Red circles are data from the same experiment as the grain size profile and are fairly well matched by the calculation.

empirical, experimentally constrained laws for a subprocess (such as annealing rates) or mechanistic models can be incorporated into the framework. In the following, we discuss (1) comparison to experimental data, (2) questions on the form of our model, (3) its relation to other analyses, and (4) application to natural conditions, in particular mantle convection and strain localization in the lithosphere.

6.1. Comparison to Experimental Data

In Figure 7, we demonstrated that we could fit the $g - \sigma$ data with one adjustable parameter (C^0_{sd}), with the prediction that there is a threshold in stress below which a temperature-dependence emerges a temperature dependence emerges due to the static grain growth term, and above which the grain size and the subgrain size converge. As discussed in section 3.1, it is possible that recrystallized grain size data from small strain compression experiments on single-crystal or coarse-grained samples may not represent the true steady state values. If the recrystallization mechanism changes, the slope could change as well. With those caveats, the possibility of a temperature dependence cannot clearly be ruled out from the data. The prediction of a stress threshold below which the slope changes and a temperature dependence emerges is a clear testable prediction. Valuable tests will come from careful analysis of mechanical and microstructural data from torsion experiments. In our illustration of this method on data from one experiment, we were able to fit the torque curve and final grain size distribution fairly well. Low strain creep and stress-relaxation tests will provide useful constraints on the microstructural evolution laws.

Furthermore, both calibration of this model and comparison to predictions of other existing models may become clearest by comparing strain-controlled and stress-controlled experiments (e.g., Hansen et al., 2012). The mechanical and thermal boundary conditions (e.g., isothermal vs. adiabatic) control the behavior of feedbacks through the microstructure and constitutive equations. For example, under strain-controlled conditions, as grain size decreases, diffusion creep rate increases, and the dislocation creep rate diminishes, so the grain size cannot be further reduced. In contrast, under constant stress conditions, as grain size decreases, the dislocation creep rate will remain constant as the diffusion creep rate increases and the total strain rate rises, increasing total dissipation. The access to thermal feedbacks (shear heating) will then strongly depend on the thermal boundary conditions. Different microstructural evolution models should make testable

predictions for experimentalists, including the sensitivity of the piezometric function to mechanical and thermal boundary conditions, even if the internal heat production cannot be directly measured.

6.2. Questions on the Model Form

As discussed in sections 1.1, 3.4.3, 3.5, and 4.4.3, the use of an attractor form of an evolution equation implies that the system in its present state has *knowledge* of some more optimal state (analogous to a chemical reaction that knows where the equilibrium state is). The FB hypothesis is compelling, but we would want that behavior to emerge, not be predetermined by an empirical grain size piezometer as the attractor (i.e., *the answer*). For near equilibrium, the notion of an attractor has a clear physical reasoning. The subgrain size as g_{att} has a direct physical link to the recrystallization process as a function of the dislocation density, discussed in section 3.5.4. That an energy balance such as the Twiss model predicts the subgrain size (Shimizu, 2008) lends credence to its role as g_{att}; the energy difference drives the kinetics. However, as discussed, g_{sg} works conceptually as the attractor only for subgrain rotation recrystallization, not for nucleation recrystallization. Changing attractors as demanded by the data is a possible means of hypothesis testing.

The treatment of dislocation dynamics we employ fits with what Cooper et al. (2016) call an *average dislocation* approach. An alternative approach to describing the behavior of the dislocation substructure combined with mechanical data is contained in the Hart mechanical equation of state and *hardness* parameter concept, as applied to rocks by, for example, Covey-Crump (1994), Stone et al. (2004), Sherburn et al. (2011), and Cooper et al. (2016). The kinetics of creep can be described by this single state variable, hardness, associated with the fractal subgrain structure, though values for olivine (Cooper et al., 2016) and halite (Stone et al., 2004) scale differently due to different dislocation dynamics (Cooper et al., 2016). The present framework can be modified to incorporate the hardness approach and simulate load relaxation tests, in order to explore different choices of microstructural state variables and candidates for g_{att}.

Finally, we do not yet have a quantitative notion of how to characterize the transition from near-equilibrium to far-from-equilibrium in this microstructural problem. This open question may be relevant in designing and interpreting experiments and also in understanding problems like postseismic relaxation in which the propagation of large stress pulses may be governed by transient creep (e.g., Freed et al., 2010). Far from equilibrium may be characterized by a situation in which the stress and the dislocation structure evolve much more quickly the than the grain boundaries can form or migrate. Nonetheless, the GSM formalism may be able to describe such situations by introducing terms into the dissipation potential for higher-stress-level dissipative mechanisms low-temperature plasticity (e.g., Kameyama et al., 1999), comminution, or cataclasis.

6.3. Comparison to Other Grain Size Evolution Models

The broad questions that have emerged in this work can be lumped into (1) the temperature dependence to steady state grain size, (2) the form of the grain size reduction term, and (3) the physical origin of the wattmeter scaling.

(1) While it is clear that the kinetics of microstructural evolution are strongly temperature dependent, the apparent lack of temperature dependence to the olivine piezometer is a conundrum. Only the Twiss model, based on equipartition of energy, does not depend on temperature. The apparent lack of temperature dependence to steady state grain size in olivine may be reassessed in experiments, in light of modern high strain torsion experiments (e.g., Bystricky et al., 2000; Hansen et al., 2012) and high-resolution electron backscatter diffraction imaging of the subgrain structure (e.g., Wallis et al., 2016). Other minerals exhibit a stronger temperature dependence (e.g., Austin & Evans, 2007; Shimizu, 2008), suggesting that the signal may be present but more subtle in olivine.

(2) As discussed in section 1.1, there are many forms of grain size evolution models, varying mainly in the form of the reduction term, $\dot{g}^{-}$, depending on some combination of σ, $\dot{\varepsilon}$, T, and g. Some incorporate an attractor (e.g., Braun et al., 1999; Kameyama et al., 1997; Montési & Hirth, 2003); the rest depend only on state variables but have some form of energy partitioning function (e.g., Behn et al., 2009; Ricard & Bercovici, 2009; Rozel et al., 2011). Explicitly incorporating the dislocation dynamics into the grain size reduction term via the subgrain size and the dislocation density is a means to physically justify the attractor and a path to incorporating much more realistic microphysical models describing recrystallization by subgrain rotation. The use of only the mean values of ρ_d and g relies on a fairly strong but common assumption that the distributions remain self-similar as the mean value evolves. Others (e.g., Hackl & Renner, 2013; Ricard & Bercovici, 2009; Rozel et al., 2011) build physically rich evolution laws that are functions of the grain size distribution, not just the mean.

While the role of the distribution in grain growth laws is relatively established (e.g., Ricard & Bercovici, 2009), incorporating dislocation density distributions into a continuum mechanistic model of dislocation dynamics and recrystallization in polycrystals is relatively open (e.g., Cooper et al., 2016; Hackl & Renner, 2013).

(3) The question of why the steady state grain size and $\dot{g}^-$ would depend on the viscous work rate $\sigma\dot{\varepsilon}_v$, rather than the stress (or strain rate) alone, was an underlying motivation for this study, as there is an intuitively appealing aspect to the idea articulated by Poliak and Jonas (1996) and Austin and Evans (2007, 2009). Rozel et al. (2011) state that the Second Law requires that grain size reduction function scale with the dissipated energy. Here we show that the use of the GSM formalism allows many forms of grain size evolution law to be consistent with the Second Law. We have only shown that scaling by dissipation is not required but have not disproven the wattmeter concept in any sense. As discussed in section 4.5, λ_{AE} (equation (53)) is identical to equation (22) in Austin and Evans (2009), but we do not use it to derive $\dot{g}_{sd}$. Thus, our result offers conceptual consistency with the wattmeter but removes the constraints on the form of $\dot{g}$ because the GSM enables a λ-free Clausius-Duhem equation (40). We demonstrate that the λ_{AE} varies widely at steady state ($0 < \lambda_{AE} < 1$) and depends on $\{T, \sigma, g, \rho_d\}$ in the current analysis. While our equation for g_{ss} (equation (57)) does not resemble the wattmeter solution, it is expected that $\dot{g}_{sd} \propto \lambda_{AE}(T, \sigma, g)\sigma\dot{\varepsilon}_{dis}$ should work as an evolution equation (assuming $\dot{\rho}_d = 0$), where the actual $\dot{g}$ function would determine the behavior of $\lambda_{AE}(T, \sigma, g)$. This point of convergence remains to be tested.

6.4. Application to Natural Settings

Microstructural evolution involving dislocations and grain size is a component in the dynamics of a vast range of settings in the solid Earth, from glacier flow to lithospheric shear zone evolution to mantle convection. Here we wish to mention briefly two questions, namely, the influence of grain size evolution on mantle convection and on strain localization in the lithosphere.

Grain size evolution during convection of materials with access to stress-, temperature-, and grain size-sensitive creep gives the system access to interesting potential feedbacks. Hall and Parmentier (2003) demonstrated that weakly deforming regions in convective cells can become stronger due to grain growth but can rapidly weaken if stressed sufficiently, due to grain size reduction. Rozel (2012) showed that convection with grain size evolution can lead to secular periodicity not accessible with temperature- and stress-dependent convection alone, due in part to memory effects reflecting grain growth. To better understand these predictions, the stress (including the pressure) dependence of grain size evolution is critical, both the rates and the steady state. The possible existence of a temperature-dependent, grain growth-dominated, steady state part of the piezometric function may lead to new expectations for grain size evolution in the convecting mantle. Much work remains to understand relationships between convection patterns, microstructure evolution, and seismically measurable properties.

For strain localization in the lithosphere, the lower-temperature and higher stress conditions lead to more rapid grain size reduction than in the asthenosphere, a process that is likely to be important in the occurrence of localized plate boundaries characteristic of plate tectonics (e.g., Jin et al., 1998; Rutter & Brodie, 1988; Vissers et al., 1995). The model in this paper is limited to quasi-static conditions but is likely to be relevant to strain localization in the lithosphere. Many modeling studies have considered the feedbacks, positive and negative, between shear heating by viscous dissipation, grain growth and grain diminution competition, and stress- and grain size-sensitive creep mechanisms (e.g., Braun et al., 1999; Foley et al., 2012; Kameyama et al., 1997; Landuyt & Bercovici, 2009; Montesi & Zuber, 2002; Regenauer-Lieb & Yuen, 1998, 2003; Thielmann, 2017). The interactions of these effects will depend on length scales and thermal boundary conditions, including the rate of heat loss relative to entropy production and the kinetics of each process. The feedbacks also depend on the mechanical boundary conditions, namely, constant displacement rate versus constant stress, the latter of which can produce unstable feedbacks more easily (e.g., Hansen et al., 2012). Here we allow for the empirical possibility of different thermal sensitivities to grain growth and diminution rates, with the impression that the latter is poorly constrained. In future work, when we analyze torsion experimental data to better constrain the scaling parameters, we will develop a reduced model with a single state variable (grain size) with behavior similar to the present model for simpler integration into geodynamic models.

7. Conclusions

We develop a set of constitutive equations to describe creep and microstructure evolution in a Maxwell-type viscoelastic material with strongly coupled thermomechanical behavior. The GSM formalism is designed to

incorporate a broad range of nonlinearity in the constitutive equations and coupling among them. In this model, dislocation density evolution (on relatively short time scales) drives grain size evolution (at longer time scales), functionally coupled by an equation of state for the subgrain size. Most subprocesses are described by empirical laws that are incorporated into the thermodynamic framework, limiting the number of unconstrained parameters. The model can reasonably fit steady state grain size data with one adjustable parameter and predicts a temperature dependence below a level of stress, but not above. Many grain size evolution models require an energy partitioning factor to determine how much of the mechanical energy is diverted from creep to microstructure evolution. In the GSM approach, by virtue of a dissipation pseudopotential and the form of the Clausius-Duhem inequality, this value is not assumed but is predicted by the model. We demonstrate how the model can be used to analyze experimental data, in particular, applied to torsional deformation experiments, in order to empirically constrain unknowns in the model and illuminate inconsistencies.

Appendix A: Dislocation Density Evolution Constraints

The following derivation allows us to extract some further empirical constraints from measurements on dislocation density evolution. We solve for the steady state conditions and set them equal to the piezometer to constrain the B_{d^+} from empirical constraints on B_{d^+}. We rearrange $\dot{\rho_d} = 0$ as

$$\rho_d^{ss} = \left(\frac{B_{d^+}}{B_{d^-}}\sigma^p\right)^{1/q} = \left(\frac{B^o_{d^+}}{B^o_{d^-}}\exp\left(\frac{\Delta Q_d}{RT}\right)\right)^{1/q}\sigma^{p/q}, \tag{A1}$$

where $\Delta Q_d = Q_{d^-} - Q_{d^+}$, recalling that we assume $B_i(T) = B_i^o \exp\left(\frac{-Q_i}{RT}\right)$. Now we can constrain values of B_{d^+} in two ways, for our present purposes without the necessary experimental data. First, if we assume that $Q_{d^-} = Q_{d^+} = 300$ (kJ/mol), we can set the definition of the steady state ρ_d defined by kinetic equations to be equal to the piezometer given in equation (23),

$$\left(\frac{B_{d^+}}{B_{d^-}}\right)^{1/q}\sigma^{p/q} = \frac{\beta}{b^2}\left(\frac{\sigma}{\mu}\right)^s. \tag{A2}$$

Then, solving for the primary unknowns and assuming that $s = p/q$, σ cancels and we obtain

$$B_{d^+} = B_{d^-}\left(\frac{\beta}{b^2\mu^s}\right)^q \tag{A3}$$

and we obtain $B^o_{d^+} = 3.6\text{E}{-6}$, as illustrated by the dashed line running through the piezometer in Figure 4b.

Alternatively, we do not assume equality of activation energies for the dislocation evolution terms in equation (A1) nor that the parameters can be constrained by the temperature-independent piezometer, as in equation (A3). We do not see a reason a priori that the rates of dislocation annihilation and production should have the same activation energy. The preexponential term will depend on the activation energies ΔQ_d and can be determined as shown in Figure 4b. It is possible that there is a weak temperature dependence to the piezometric data that cannot be ruled out, as illustrated in Figure 4b; for the temperature range of 400 °C, and $\Delta Q_d = \pm 50$ (kJ/mol), there is a small finite width to the predictions that may be within experimental uncertainty, but a large change in the value of $B^o_{d^+}$ required to bring the fits back toward the data. Thus, we leave these questions to be pursued in future empirical studies.

Appendix B: Mechanics of Torsion Experiments

As discussed in the text, all state variables and parameters can be tensorial, but we restrict this analysis to scalar values. How that reduction occurs depends on the type of experiment being considered. For example, in a uniaxial compression test, the stress tensor σ is reduced to the differential stress, $\sigma = \sigma_1 - \sigma_3 = 2\tau$, where the single subscripts indicate the eigenvalues of the principal stress tensor of any σ_{ij}. The τ is the magnitude of the shear stress.

Torsional deformation creates a complex stress distribution in the sample. We want to be able to interpret both the macroscopic mechanical behavior, that is, the measured torque as well as the microstructures. As shown in Figure 12a, we use the symbols and terminology of Paterson and Olgaard (2000), who were primarily concerned with the relationship between stress and strain in torsion samples with those in the uniaxial compression samples in which the flow laws are determined. In uniaxial compression, the *equivalent stress* is

the differential stress. Their conclusion for torsion was that $\sigma_{eq} = \sqrt{3}\tau$ and $\varepsilon_{eq} = \frac{\gamma}{\sqrt{3}}$. The measured torque is $\mathcal{M} = 2\pi \int \tau_r r^2 dr$ and in time $\mathcal{M}(t) = 2\pi \int \tau_r(t) r^2 dr$.

B1. Zero-Dimensional Simplification for Analysis of Large Strain Experiments

As illustrated in Figure 12, we consider each finite width annulus of the torsion sample to be a single homogeneous 0-D model. The question is the relationship of the scalar value for strain that we integrate and the actual strain in the torsion sample at a given point. To calculate the strain rate tensor for torsion, we start with the velocity field at point m: $v_i = [v_r, v_\theta, v_z] = \left[0, \frac{r\dot{\theta}z}{h}, 0\right]$, where h is the height of the sample. The velocity gradient tensor $G = \nabla v_i$ and the strain rate tensor $D = \frac{1}{2}\left(G + G^T\right)$. The nonzero components of D are $D_{\theta z} = \dot{\gamma}$ and $D_{z\theta} = \dot{\gamma}$, where $\dot{\gamma} = \frac{r\dot{\theta}}{2h}$. Thus, there are no components in the strain tensor that are affected by the large strain or complicate the relationship between what we integrate and the mechanical properties; at any moment, the strains and strain rates are simply related by $\sigma_{eq} = \sqrt{3}\tau$, which we incorporate in the calculations. Note that this approximation does not hold for simple shear; the circular rotation of the torsion sample removes the component of the stress tensor that causes rotation of stress with large strain in simple shear.

An important criterion for the reduction of the torsion to quasi-1-D is that we are not violating mechanical equilibrium by treating each annulus as an independent model in terms of stress (they are only *connected* by the linear increase in the imposed shear strain rate from center to edge. Violating mechanical equilibrium would mean that there are gradients stress components that must be non-nul and calculated. Because there is no $\frac{\partial \sigma_{\theta z}}{\partial r}$ component in the equilibrium statement for torsional deformation, the approximation of torsion as concentric annuli does not violate mechanical equilibrium (Germain et al., 1983).

B2. Thermal Time Constant of the Paterson Machine

For this study, we estimate this time constant empirically from the measured thermal relaxation curves for the Paterson gas-medium deformation apparatus. The thermal relaxation constant τ_{th} is the time for the temperature to reach $1/e$ of its initial value. In this case, from 1473 to 541 K, takes about 700 s (L. Hansen, personal communication, December 23, 2012). This value is probably an upper bound because it is measured when the furnace is switched off, such that convection of argon gas around the sample is decreasing in vigor (A. Quintanilla Terminel, personal communication, March 13, 2012).

Acknowledgments

The seed for the this collaboration was planted when B. K. H. sat in the back of A. C.'s course on Thermomechanics at the Université de Montpellier II, Fall 2000. B. K. H. dedicates this paper to his father, David Holtzman, who took a class on the TIP with Prigogine in 1964 and nudged this project along over its 7 years while resisting the Second Law. We also thank B. Evans, R. Cooper, D. Mainprice, L. Hansen, A. Tommasi, C. Thoraval, D. Kohlstedt, G. Hirth, K. Regenauer-Lieb, H. Lau, and A. Quintanilla Terminel for helpful discussions and O. et F. Hallé for logistical support in Montpellier. We thank D. Bercovici, Y. Ricard, and J. Wheeler for their critical, helpful reviews. Funding was provided by NSF grant EAR 11-41976 and NSF CAREER grant EAR 10-56332 to B. K. H. and by LMGC. Data access statement: This paper, being theoretical, reports no new data. LDEO contribution 8254.

References

Austin, N. J., & Evans, B. (2007). Paleowattmeters: A scaling relation for dynamically recrystallized grain size. *Geology*, *35*(4), 343. https://doi.org/10.1130/G23244A.1

Austin, N., & Evans, B. (2009). The kinetics of microstructural evolution during deformation of calcite. *Journal of Geophysical Research*, *114*, B09402. https://doi.org/10.1029/2008JB006138

Bai, Q., & Kohlstedt, D. L. (1992). High-temperature creep of olivine single-crystals. 2. Dislocation-structures. *Tectonophysics*, *206*, 1–29.

Behn, M. D., Hirth, G., & Ii, J. R. E. (2009). Implications of grain size evolution on the seismic structure of the oceanic upper mantle. *Earth and Planetary Science Letters*, *282*, 178–189. https://doi.org/10.1016/j.epsl.2009.03.014

Bercovici, D., Ricard, Y., & Schubert, G. (2001). A two-phase model for compaction and damage: 1. General theory. *Journal of Geophysical Research*, *106*(B5), 8887–8906.

Boioli, F., Carrez, P., Cordier, P., Devincre, B., & Marquille, M. (2015). Modeling the creep properties of olivine by 2.5-dimensional dislocation dynamics simulations. *Physical Review B*, *92*(1), 014115.

Braun, J., Chéry, J., Poliakov, A., Mainprice, D., Vauchez, A., Tomassi, A., et al. (1999). A simple parameterization of strain localization in the ductile regime due to grain size reduction: A case study for olivine. *Journal of Geophysical Research*, *104*(B11), 25,167–25,181.

Bystricky, M., Kunze, K., Burlini, L., & Burg, J. (2000). High shear strain of olivine aggregates: Rheological and seismic consequences. *Science*, *290*(5496), 1564.

Chrysochoos, A. (1985). Energy balance for elastic-plastic deformation at finite strain. *Journal de Mé,canique théorique et appliquée*, *4*(5), 589–614.

Chrysochoos, A., Berthel, B., Latourte, F., Pagano, S., Wattrisse, B., & Weber, B. (2008). Local energy approach to steel fatigue. *Strain*, *44*(4), 327–334.

Chrysochoos, A., Löbel, M., & Maisonneuve, O. (1995). Couplages thermomécaniques du comportement pseudoélastique d'alliages cu-zn-al et ni-ti. *Comptes rendus de l'Académie des sciences. Série II Mé,canique, physique, chimie, astronomie*, *320*(5), 217–223.

Chrysochoos, A., & Louche, H. (2000). An infrared image processing to analyse the calorific effects accompanying strain localisation. *International Journal of Engineering Science*, *38*(16), 1759–1788. https://doi.org/10.1016/S0020-7225(00)00002-1

Chrysochoos, A., Maisonneuve, O., Martin, G., Caumon, H., & Chezeaux, J. (1989). Plastic and dissipated work and stored energy. *Nuclear Engineering and Design*, *114*(3), 323–333.

Coleman, B. D., & Noll, W. (1963). The thermodynamics of elastic materials with heat conduction and viscosity. *Archive for Rational Mechanics and Analysis*, *13*(1), 167–178.

Cooper, R. F., Stone, D. S., & Plookphol, T. (2016). Load relaxation of olivine single crystals. *Journal of Geophysical Research: Solid Earth*, *121*, 7193–7210. https://doi.org/10.1002/2016JB013425

Covey-Crump, S. J. (1994). The application of Hart's state variable description of inelastic deformation to Carrara marble at $T < 450$ °C. *Journal of Geophysical Research*, *99*(B10), 19,793–19,808.

de Bresser, J., Peach, C., Reijs, J., & Spiers, C. (1998). On dynamic recrystallization during solid state flow: Effects of stress and temperature. *Geophysical Research Letters*, *25*(18), 3457–3460.

de Bresser, J. H., Ter Heege, J., & Spiers, C. (2001). Grain size reduction by dynamic recrystallization: Can it result in major rheological weakening? *International Journal of Earth Sciences*, *90*(1), 28–45.
De Groot, S. R., & Mazur, P. (1984). *Non-equilibrium thermodynamics, Dover Books*. Amstedam: North Holland Pub. Co.
Derby, B. (1991). The dependence of grain size on stress during dynamic recrystallisation. *Acta metallurgica et materialia*, *39*(5), 955–962.
Derby, B., & Ashby, M. (1987). On dynamic recrystallisation. *Scripta Metallurgica*, *21*(6), 879–884.
Durham, W., & Goetze, C. (1977). Plastic flow of oriented single crystals of olivine: 1. Mechanical data. *Journal of Geophysical Research*, *82*(36), 5737–5753.
Durham, W., Goetze, C., & Blake, B. (1977). Plastic flow of oriented single crystals of olivine: 2. Observations and interpretations of the dislocation structures. *Journal of Geophysical Research*, *82*(36), 5755–5770.
Evans, B., Renner, J., & Hirth, G. (2001). A few remarks on the kinetics of static grain growth in rocks. *International Journal Of Earth Sciences*, *90*(1), 88–103.
Foley, B. J., Bercovici, D., & Landuyt, W. (2012). The conditions for plate tectonics on super-earths: Inferences from convection models with damage. *Earth and Planetary Science Letters*, *331*, 281–290.
Freed, A. M., Herring, T., & Bürgmann, R. (2010). Steady-state laboratory flow laws alone fail to explain postseismic observations. *Earth and Planetary Science Letters*, *300*(1-2), 1–10.
Germain, P., Nguyen, Q. S., & Suquet, P. (1983). Continuum thermodynamics. *Journal of Applied Mechanics-Transactions of the Asme*, *50*(4B), 1010–1020.
Goetze, C., & Kohlstedt, D. (1973). Laboratory study of dislocation climb and diffusion in olivine. *Journal of Geophysical Research*, *78*(26), 5961–5971.
Guillope, M., & Poirier, J. (1979). Dynamic recrystallization during creep of single-crystalline halite: An experimental study. *Journal of Geophysical Research*, *84*(B10), 5557–5567.
Hackl, K., & Renner, J. (2013). High-temperature deformation and recrystallization: A variational analysis and its application to olivine aggregates. *Journal of Geophysical Research: Solid Earth*, *118*, 943–967. https://doi.org/10.1002/jgrb.50125
Hall, C. E., & Parmentier, E. M. (2003). Influence of grain-size evolution on convective instability. *Geochemistry, Geophysics, Geosystems*, *4*(3), 27. https://doi.org/10.1029/2002GC000308
Halphen, B., & Nguyen, Q. S. (1975). Sur les maté,riaux standard généralisés. *Journal de mécanique*, *14*, 39–63.
Hansen, L. N., & Warren, J. M. (2015). Quantifying the effect of pyroxene on deformation of peridotite in a natural shear zone. *Journal of Geophysical Research: Solid Earth*, *120*, 2717–2738. https://doi.org/10.1002/2014JB011584
Hansen, L. N., Zimmerman, M. E., Dillman, A. M., & Kohlstedt, D. L. (2012). Strain localization in olivine aggregates at high temperature: A laboratory comparison of constant-strain-rate and constant-stress boundary conditions. *Earth and Planetary Science Letters*, *333-334*(C), 134–145. https://doi.org/10.1016/j.epsl.2012.04.016
Hansen, L. N., Zimmerman, M. E., & Kohlstedt, D. L. (2011). Grain boundary sliding in San Carlos olivine: Flow law parameters and crystallographic-preferred orientation. *Journal of Geophysical Research*, *116*, 201. https://doi.org/10.1029/2011JB008220
Herwegh, M., Poulet, T., Karrech, A., & Regenauer-Lieb, K. (2014). From transient to steady state deformation and grain size: A thermodynamic approach using elasto-visco-plastic numerical modeling. *Journal of Geophysical Research: Solid Earth*, *119*, 900–918. https://doi.org/10.1002/2013JB010701
Hiraga, T., Tachibana, C., Ohashi, N., & Sano, S. (2010). Grain growth systematics for forsterite +/− enstatite aggregates: Effect of lithology on grain size in the upper mantle. *Earth And Planetary Science Letters*, *291*, 10–20.
Hirth, G., & Kohlstedt, D. L. (2003). Rheology of the upper mantle and the mantle wedge: A view from the experimentalists. *Geophysical Monograph Series*, *138*, 83–105.
Hirth, G., & Kohlstedt, D. (2015). The stress dependence of olivine creep rate: Implications for extrapolation of lab data and interpretation of recrystallized grain size. *Earth and Planetary Science Letters*, *418*, 20–26.
Jin, D., Karato, S.-i., & Obata, M. (1998). Mechanisms of shear localization in the continental lithosphere: Inference from the deformation microstructures of peridotites from the ivrea zone, northwestern Italy. *Journal of Structural Geology*, *20*(2-3), 195–209.
Kameyama, M., Yuen, D., & Fujimoto, H. (1997). The interaction of viscous heating with grain-size dependent rheology in the formation of localized slip zones. *Geophysical Research Letters*, *24*(20), 2523–2526.
Kameyama, M., Yuen, D. A., & Karato, S.-I. (1999). Thermal-mechanical effects of low-temperature plasticity (the Peierls mechanism) on the deformation of a viscoelastic shear zone. *Earth and Planetary Science Letters*, *168*(1), 159–172.
Karato, S. (1989). Grain growth kinetics in olivine aggregates. *Tectonophysics*, *168*, 255–273.
Karato, S.-I., & Jung, H. (2003). Effects of pressure on high-temperature dislocation creep in olivine. *Philosophical Magazine*, *83*(3), 401–414.
Karato, S., & Toriumi, M. (1980). Dynamic recrystallization of olivine single crystals during high-temperature creep. *Geophysical Research Letters*, *7*, 649–652.
Karrech, A., Regenauer-Lieb, K., & Poulet, T. (2011). Continuum damage mechanics for the lithosphere. *Journal Of Geophysical Research*, *116*, B04205. https://doi.org/10.1029/2010JB007501
Kellermann Slotemaker, A., & De Bresser, J. (2006). On the role of grain topology in dynamic grain growth — 2D microstructural modeling. *Tectonophysics*, *427*(1), 73–93.
Kellermann Slotemaker, A., De Bresser, J. H. P., Spiers, C. J., & Drury, M. R. (2004). Microstructural evolution of synthetic forsterite aggregates deformed to high strain. In *Materials Science Forum* (Vol. 467, pp. 579-584). Trans Tech Publ.
Kidder, S., Hirth, G., Avouac, J.-P., & Behr, W. (2016). The influence of stress history on the grain size and microstructure of experimentally deformed quartzite. *Journal of Structural Geology*, *83*, 194–206.
Kohlstedt, D., Nichols, H., & Hornack, P. (1980). The effect of pressure on the rate of dislocation recovery in olivine. *Journal of Geophysical Research*, *85*(B6), 3122–3130.
Landuyt, W., & Bercovici, D. (2009). Formation and structure of lithospheric shear zones with damage. *Physics of the Earth and Planetary Interiors*, *175*(3-4), 115–126.
Li, L., Muracciole, J.-M., Waltz, L., Sabatier, L., Barou, F., & Wattrisse, B. (2016). Local experimental investigations of the thermomechanical behavior of a coarse-grained aluminum multicrystal using combined DIC and IRT methods. *Optics and Lasers in Engineering*, *81*, 1–10.
Montési, L. G., & Hirth, G. (2003). Grain-size evolution and the rheology of ductile shear zones: From laboratory experiments to postseismic creep. *Earth and Planetary Science Letters*, *211*(1-2), 97–110. https://doi.org/10.1016/S0012-821X(03)00196-1
Montesi, L., & Zuber, M. T. (2002). A unified description of localization for application to large-scale tectonics. *Journal of Geophysical Research*, *107*(B3), 2045. https://doi.org/10.1029/2001JB000465
Paterson, M., & Olgaard, D. (2000). Rock deformation tests to large shear strains in torsion. *Journal of Structural Geology*, *22*(9), 1341–1358.
Phillpot, S. R., Wolf, D., & Yip, S. (1990). Effects of atomic-Level disorder at solid interfaces. *MRS Bulletin*, *15*(10), 38–45. https://doi.org/10.1557/S0883769400058656

Poliak, E., & Jonas, J. (1996). A one-parameter approach to determining the critical conditions for the initiation of dynamic recrystallization. *Acta Materialia*, *44*(1), 127–136.
Precigout, J., Gueydan, F., Gapais, D., Garrido, C., & Essaifi, A. (2007). Strain localisation in the subcontinental mantle—A ductile alternative to the brittle mantle. *Tectonophysics*, *445*(3-4), 318–336.
Regenauer-Lieb, K., & Yuen, D. (1998). Rapid conversion of elastic energy into plastic shear heating during incipient necking of the lithosphere. *Geophysical Research Letters*, *25*(14), 2737–2740.
Regenauer-Lieb, K., & Yuen, D. (2003). Modeling shear zones in geological and planetary sciences: Solid-and fluid-thermal–mechanical approaches. *Earth-Science Reviews*, *63*(3-4), 295–349.
Ricard, Y., & Bercovici, D. (2009). A continuum theory of grain size evolution and damage. *Journal Of Geophysical Research*, *114*, B01204. https://doi.org/10.1029/2007JB005491
Rittel, D. (1999). On the conversion of plastic work to heat during high strain rate deformation of glassy polymers. *Mechanics of Materials*, *31*(2), 131–139.
Rittel, D., & Zhang, L. S. (2017). The dependence of the Taylor-Quinney coefficient on the dynamic loading mode. *Journal of the Mechanics and Physics of Solids*, *107*, 96–114.
Rozel, A. (2012). Impact of grain size on the convection of terrestrial planets. *Geochemistry, Geophysics, Geosystems*, *13*, Q10020. https://doi.org/10.1029/2012GC004282
Rozel, A., Ricard, Y., & Bercovici, D. (2011). A thermodynamically self-consistent damage equation for grain-size evolution during dynamic recrystallization. *Geophysical Journal International*, *184*(2), 719–728.
Rutter, E. H. (1995). Experimental study of the influence of stress, temperature, and strain on the dynamic recrystallization of Carrara marble. *Journal of Geophysical Research*, *100*(B12), 24,651–24,663.
Rutter, E., & Brodie, K. (1988). The role of tectonic grain size reduction in the rheological stratification of the lithosphere. *Geologische Rundschau*, *77*(1), 295–307.
Sherburn, J., Horstemeyer, M., Bammann, D., & Baumgardner, J. (2011). Application of the Bammann inelasticity internal state variable constitutive model to geological materials. *Geophysical Journal International*, *184*(3), 1023–1036.
Shimizu, I. (1998). Stress and temperature dependence of recrystallized grain size: A subgrain misorientation model. *Geophysical Research Letters*, *25*(22), 4237–4240.
Shimizu, I. (2008). Theories and applicability of grain size piezometers: The role of dynamic recrystallization mechanisms. *Journal of Structural Geology*, *30*(7), 899–917.
Stipp, M., & Tullis, J. (2003). The recrystallized grain size piezometer for quartz. *Geophysical Research Letters*, *30*(21), 2088. https://doi.org/10.1029/2003GL018444
Stipp, M., Tullis, J., & Behrens, H. (2006). Effect of water on the dislocation creep microstructure and flow stress of quartz and implications for the recrystallized grain size piezometer. *Journal of Geophysical Research*, *111*, B04201. https://doi.org/10.1029/2005JB003852
Stipp, M., Tullis, J., Scherwath, M., & Behrmann, J. H. (2010). A new perspective on paleopiezometry: Dynamically recrystallized grain size distributions indicate mechanism changes. *Geology*, *38*(8), 759–762.
Stone, D. S., Plookphol, T., & Cooper, R. F. (2004). Similarity and scaling in creep and load relaxation of single-crystal halite (NaCl). *Journal of Geophysical Research*, *109*, B12201. https://doi.org/10.1029/2004JB003064
Tasaka, M., & Hiraga, T. (2013). Influence of mineral fraction on the rheological properties of forsterite+ enstatite during grain-size-sensitive creep: 1. Grain size and grain growth laws. *Journal of Geophysical Research: Solid Earth*, *118*, 3970–3990. https://doi.org/10.1002/jgrb.50285
Taylor, G. I., & Quinney, H. (1934). The latent energy remaining in a metal after cold working, Proceedings of the Royal Society of London. Series A. *Containing Papers of a Mathematical and Physical Character*, *143*(849), 307–326.
Thielmann, M. (2017). Grain size assisted thermal runaway as a nucleation mechanism for continental mantle earthquakes, Impact of complex rheologies, Tectonophysics.
Tolman, R. C., & Fine, P. C. (1948). On the irreversible production of entropy. *Reviews of Modern Physics*, *20*(1), 51.
Tommasi, A., Vauchez, A., Femandes, L., & Porcher, C. (1994). Magma-assisted strain localization in an orogen-parallel transcurrent shear zone of southern Brazil. *Tectonics*, *13*(2), 421–437.
Toriumi, M. (1979). Relation between dislocation density and subgrain size of naturally deformed olivine in peridotites. *Contributions to Mineralogy and Petrology*, *68*(2), 181–186.
Toriumi, M. (1982). Grain boundary migration in olivine at atmospheric pressure. *Physics of The Earth and Planetary Interiors*, *30*(1), 26–35.
Truesdell, C. (1969). *Rational thermodynamics: A course of lectures on selected topics*. New York: McGraw-Hill.
Twiss, R. J. (1977). Theory and applicability of a recrystallized grain size paleopiezometer. *Pure And Applied Geophysics*, *115*(1-2), 227–244.
van der Wal, D., Chopra, P., Drury, M., & Gerald, J. (1993). Relationships between dynamically recrystallized grain size and deformation conditions in experimentally deformed olivine rocks. *Geophysical Research Letters*, *20*(14), 1479–1482.
Vissers, R., Drury, M., Hoogerduijn, E., Spiers, C., Van der Wal, D., et al. (1995). Mantle shear zones and their effect on lithosphere strength during continental breakup. *Tectonophysics*, *249*(3-4), 155–171.
Wallis, D., Hansen, L. N., Britton, T. B., & Wilkinson, A. J. (2016). Geometrically necessary dislocation densities in olivine obtained using high-angular resolution electron backscatter diffraction. *Ultramicroscopy*, *168*, 34–45.